Materials & Design 250 (2025) 113627

Contents lists available at ScienceDirect

Materials & Design

journal homepage: www.elsevier.com/locate/matdes

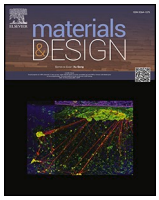

Tailoring the strength of inconel 718: Insights into LPBF parameters and heat treatment synergy

Galina Kasperovich [a,*], Joachim Gussone [a], Guillermo Requena [a,b], Norbert Schell [c], Andreas Stark [c], Jan Haubrich [a]

[a] German Aerospace Center (DLR), Institute of Materials Research, Linder Hoehe 51147 Cologne, Germany
[b] RWTH Aachen University, Metallic Structures and Materials Systems for Aerospace Engineering 52062 Aachen, Germany
[c] Helmholtz-Zentrum Hereon, Institute of Materials Physics, Max-Planck-Straße 1 21502 Geesthacht, Germany

ARTICLE INFO

Keywords:
Inconel 718
Laser powder bed fusion
Heat treatment
Precipitation
High energy synchrotron diffraction

ABSTRACT

The enhancement of mechanical performance in Inconel 718 fabricated via Laser Powder Bed Fusion by optimizing process parameters and various post-processing heat treatments, such as double aging and high-temperature isostatic pressing, are explored. Phase and texture evolution were characterized by high-energy diffraction electron backscatter diffraction analysis, showing a weak Goss-type texture in the as-built condition. Carrying out a homogenization annealing above δ solvus, e.g. at 1155 °C, suppresses its transformation into δ phase and enables an aging treatment to achieve a controlled precipitation of γ'/γ'' instead. MC-type carbides were detected in different morphologies at grain boundaries and in the matrix. Linking the microstructural changes with trends in the tensile properties along three build orientations, i.e. horizontal, diagonal and vertical to the build platform, we show that texture and anisotropy in the as-built condition can largely be eliminated by an annealing at 1155 °C. The mechanical properties can be adjusted further by adding double-aging or varying the cooling rate after the solvus treatment. The findings reveal a clear correlation between optimized LPBF parameters, heat treatment strategies, microstructural evolution, phase distribution, and the resultant mechanical properties, which contributes to the development of tailored process chains for specific application requirements.

1. Introduction

Additive manufacturing (AM) techniques such as Laser-based Powder Bed Fusion (LPBF or PBF-LB/M) of metallic alloys enable the production of highly complex components with exceptional customization or integration of multi-part assemblies into one structure [1–5]. For gas turbines in aeronautics, the LPBF technology has gained particular attention due to its ability to produce high pressure turbine vanes with intricate internal cooling structures. AM, thus is maturing to a new, more flexible alternative to casting technologies. The precise fabrication of such intricate geometries by LPBF is critical for aerospace components [6–9].

Among the high-temperature alloys with good processability in laser-welding-based processes, Inconel 718 (IN718) is widely employed and investigated. IN718 is a nickel–chromium-iron-based precipitate-strengthened superalloy commonly used for gas turbine components in jet engines due to its favorable mechanical properties and corrosion resistance at elevated temperatures up to approximately 650–700 °C [10–13].

The microstructures of LPBF materials including grain morphology and texture are influenced directly by the processing parameters and scan strategies that affect the solidification process. Poorly optimized build parameters can lead to unintended loss of alloying elements, high residual stresses, or significant porosity and fusion defects, all of which generally impair the mechanical properties [14–18]. While the influence of individual LPBF printing parameters on properties such as hardness, surface roughness, and strength has been explored in various works [19–21], the correlations between mechanical properties, e.g. strength, and processing parameters is still being discussed controversially due to the complex and numerous influence factors.

The principal microstructural constituents of IN718 are the γ-matrix (a supersaturated solid solution phase with an fcc lattice structure, A_1) and various phases whose composition and fraction depend on the processing route and heat treatment history. Optimizing the coherent

* Corresponding author.
E-mail address: galina.kasperovich@dlr.de (G. Kasperovich).

https://doi.org/10.1016/j.matdes.2025.113627
Received 16 October 2024; Received in revised form 28 November 2024; Accepted 14 January 2025
Available online 22 January 2025

strengthening γ' (Ni_3(Al, Ti, Nb, fcc, L_{12})) and γ'' (Ni_3Nb, bct, DO_{22}) phases by heat treatments while minimizing detrimental precipitates is crucial for high strength characteristics. Precipitates like Laves and the δ phases need to be avoided. A combination of solution annealing (S), homogenization (H), or hot-isostatic pressing (HIP) and double-aging (DA) is commonly used (e.g.[12,22]).

Differential scanning calorimetry (DSC) and differential thermal analysis (DTA) generally revealed the following solid-state phase transformations during annealing of IN718:

- precipitation of γ' around ~ 500°C [22] to 565°C [23,24],
- precipitation of γ'' around 700 °C [22] to 740°C [24] or even 755 °C [23],
- precipitation of δ around 850 °C [22], 870 °C [24] / 880 °C [23]
- and dissolution of metastable phases including a Laves phase in endothermic transformations with a wide temperature range between ~ 950 °C and ~ 1070 °C [22–24].

The temperature ranges determined using DSC by Bassini et al. [23], Calandri et al. [24] or DTA by Niang et al. [22] are in good agreement and, thus, can also be expected to apply to the as-built state of LPBF IN718.

After rapid solidification in LPBF, the formation of a coarse-grained Laves phase (Ni, Cr, Fe)$_2$(Nb, Mo, Ti) on γ-grain boundaries has been observed and found to negatively affect mechanical properties causing cracking in the as-built state [25–27]. This brittle Laves phase has been reported to convert at temperatures above 650 °C into the orthorhombic δ-phase (Ni_3Nb, $D0_a$), which can also form intragranularly in contrast to the Laves phase[25–45]. Neither phase favours the mechanical performance of the LPBF material [25–45]. The δ solvus, in line with the temperature range given above, has been determined to correspond to 980–1050 °C [38,49,50]. In order to dissolve the undesired Laves-phase and, partially the δ-phase, an initial solutionizing step (S) is often performed at temperatures around 850 °C to 1000 °C [21,31–42] and [47,48]. This is often followed by annealing at 1020 °C to 1165 °C to homogenize alloying element distribution (H) and induce recrystallization [6,37–45,48]. Simultaneously, these treatments promote the precipitation of γ' and γ'', thus improving strength [39]. Subsequent double-aging treatment (H + DA) allows achieving maximum yield and ultimate tensile strengths [6,37–45,48]. In combination with isostatic pressing (HIP), these heat treatments can also heal internal defects such as porosity [34–36,46,51].

Moreover, LPBF IN718 also contains primary MC-type carbides (e.g. (Nb, Ti)C), which are usually present both in the matrix and at grain boundaries and affect elongation detrimentally [32,52,53]. Unlike the δ and Laves phases, MC-type carbides in IN718 are stable at high temperatures [10] and have even been found to coarsen significantly during high temperature annealing up to 1100–1120 °C, when they also enrich in Nb and Ti and deplete in Ni, Fe, and Cr [52].

Therefore, the annealing temperatures and times for the solutionizing and homogenization must be optimized and balanced with care. Heat treatments below the δ solvus, on the one hand, can transform the Laves phase into the δ phase, capturing Nb and Ti and reducing the availability for forming γ' and γ''. Thereby an unfavorable microstructure neither optimizing the strength not retaining a high ductility may result [26,41]. On the other hand, too long or too high annealing temperatures can reduce the material's ductility due to the growth of carbides.

Of particular interest for additively manufactured materials is the question of texture since it can lead to substantial anisotropy in the mechanical properties. Such an anisotropy typically complicates the design and sizing of of components. Especially in LPBF, whence the heat dissipation can follow the actual geometry of the printed parts to the base platform, the texture can vary locally and requires a thorough understanding. The textures reported in the literature vary strongly with respect to texture type and intensity. Most studies of as-built LPBF IN718 materials report a preferred ⟨001⟩ grain orientation with columnar grains in build direction that is usually attributed to the thermal gradient during the rapid cooling [28,34–36,54–56].

However, other investigations of LPBF processed IN718 have also reported qualitatively distinctive textures: Goss-type {110} ⟨001⟩ for single-crystal-like, crystallographic lamellar and polycrystalline microstructures [55] or Cube {001} ⟨001⟩ [28,56]. The texture intensities range from weak textures with maximum multiple of uniform density (MUD) values below 3 [39] to strong textures with MUD_{max} above 10 [56]. In addition, many studies reported substantial differences in the plastic and elastic properties as function of build direction. The corresponding explanations vary between micromechanical (crystallographic orientation of the active slip systems) as well as microstructural (lattice defects) reasons or thermal eigenstresses as origin.

In order to further the understanding in the material behavior of LPBF IN718 in the as-built condition and after typical heat treatments, this study systematically explores the influence of LPBF process strategies and thermal postprocessing on the microstructures, phase compositions, texture evolution and on the mechanical properties of LPBF IN718. A wide range of LPBF process parameters are studied to minimize porosity and compared with data obtained by other authors using different LPBF systems. Qualitative phase analysis using high-energy synchrotron X-ray diffraction (HEXRD) was conducted to identify small-scale Laves precipitates, δ phase, carbides, and γ''. The microstructures and phase analyses of different LPBF IN718 conditions before and after heat treatments are correlated with room temperature tensile properties obtained from specimens oriented at 0° (horizontal), 45° (diagonal), and 90° (vertical), considering microstructure and texture formation during rapid solidification. Finally, a comparison and discussion of the observed trends in view of the vast literature on LPBF of IN718 is carried out, aiming at providing a more complete overview of the LPBF material processed with different parameters and heat treatments.

The novelty of this work lies in the comprehensive experimental data on the microstructural evolution and mechanical properties of LPBF IN718 alloy in both the as built and various thermo-mechanically treated states. By correlating the optimized LPBF parameters, microstructures, phase evolution, and mechanical properties, this study provides new insights into tailoring material performance. The comparative analysis with existing literature further highlights the significant advancements achieved in optimizing strength and ductility for critical applications.

2. Experimental methods

2.1. IN718 powder feedstock

IN718 alloy powder was purchased from AP&C (Boisbriand, Canada). It was produced by plasma atomization in a high purity argon atmosphere, resulting in mostly spherical particles. The particle size distribution, measured by a particle size analyser (LS 13,320 PIDS, Beckman Coulter), has D-values of 22 μm (D10), 33 μm (D50) and 45 μm (D90) (Fig. 1 (a)). The chemical powder composition analyzed by means of X-ray fluorescence analysis (XRF) at RevierLabor© (Essen, Germany) is given in a Table 1**.** The powder complies with the regulation AMS5662 [57]. Initially, the powder was characterized by some bulk porosity as shown in the cross section of the particles: metallographic image of particles without and with porosity – Fig. 1 (b and c, respectively).

2.2. LPBF method

A Concept Laser M2 machine (Concept Laser GmbH, Lichtenfels, Germany) equipped with a 200 W diode-pumped ytterbium fibre laser, operating in continuous wave-mode with a Gaussian beam shape, was used to manufacture the LPBF specimens. A chess-pattern laser scan strategy was used with an island size of 5 × 5 mm^2, and the scanning

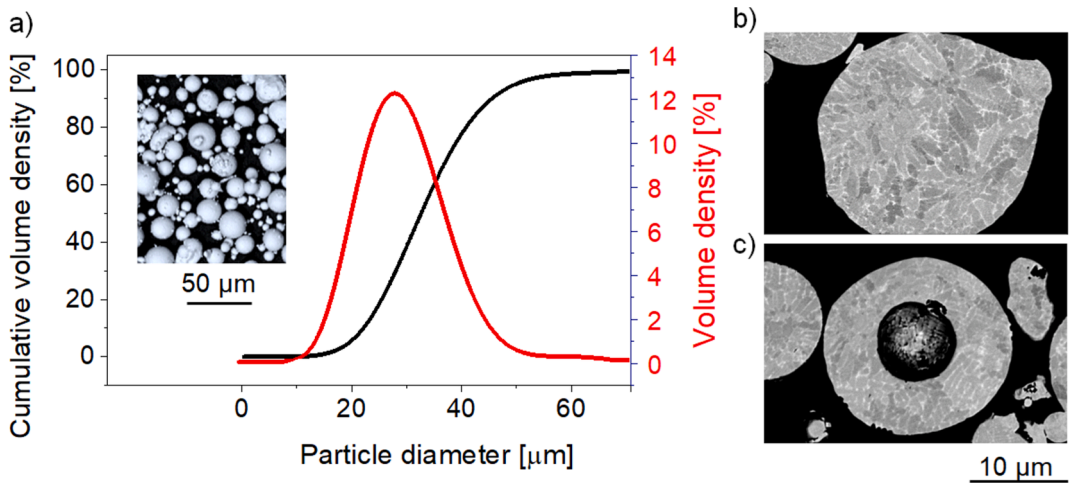

Fig. 1. IN718 powder particle distribution (a), metallographic image of powder particles showing internal dendritic microstructure without (b) and with (c) internal porosity.

Table 1
Composition (wt. %) of the IN718 alloy powder measured by XRF.

Ni	Cr	Fe	Nb	Mo	Ti	Al	Co	Mn	C
Bal.	18.70	18.49	5.30	2.93	0.95	0.42	0.03	0.07	0.042

directions (45° inclined to the bidirectional recoating) rotated 90° from one layer to the next.

2.3. Porosity analysis for the optimization of LPBF process parameters

A process window for obtaining the maximum material density, i.e. lowest residual porosity and elimination of cracking phenomena, was developed based on the analysis of cubic samples of 10 × 10 × 10 mm^3. In total, more than 200 cubes were produced varying laser power P, scanning speed v, and hatch distance h at a fixed powder layer thickness of t = 30 μm. The resulting energy densities $E_v = P / (v \times h \times t)$ ranged from 30 to 300 J/mm^3. The layer thickness was selected with respect to the manufacturing of turbine blade demonstrators with coolant channels that require a fine degree of high structural resolution.

The porosity of the cubic samples was investigated by two ways: the Archimedes method and the two-dimensional (2D) image processing technique.

In the Archimedes method, porosity was measured by weighing in ethanol using a KERN® ABT analytical balance and calculated with an assumed nominal density of IN718 of 8.193 g/cm^3 with correction for temperature-dependent liquid density. Each sample was measured at least three times and the values obtained were averaged.

Using 2D image processing, the porosity was quantified from metallographic sections parallel to the LPBF build direction (**Fig. S1** in the Supplementary Material). The metallographic sections were initially ground with SiC sandpaper to 4000 grit and then polished with a SiO_2-H_2O_2 suspension. Visualization was performed on a ZEISS® LSM 700 at 100 × magnification with a PILine® scanning workstation using the stitching function of the ZEN 2012 software (black edition) [58]. The porosity in the images was analyzed and quantified using the software package AnalySIS [59].

The cross-sectional areas examined were approximately 9.5 × 9.5 mm^2 for each sample, and 3 different parallel sections of each sample were evaluated to determine the average porosity for each parameter set. Edge areas of the cross sections, which may have specific defects caused, for example, by overheating, were not included in the determination of volumetric porosity. The 2D images were also used to classify the type of defects depending on the laser process parameters used.

2.4. Tensile testing program

Optimized LPBF parameters from the porosity study (Section 3.1) were used to produce specimens for mechanical testing. Tensile tests at room temperature assessed ultimate and yield strengths and trends in the strength-ductility balance. A custom specimen geometry was developed for cyclic and monotonic testing, minimizing bending effects (Fig. 2). Its gauge diameter-to-length ratio, below ASTM E8/E8M-11 standards, may increase elongation at fracture, requiring cautious comparison with literature data. However, trends in the mechanical performance after heat-treatment remain valid.

Fifty-four cylinders (16 mm diameter, 80 mm length) were produced using optimized parameters ($E_{V,opt}$ = 60 J/mm^3, Section 3.1) in three build orientations: 18 each at 0°, 45°, and 90° (Fig. 1(b)). Three additional vertical samples were printed with standard IN718 parameters (180 W, 600 mm/s, 0.105 mm hatch, $E_{V,in}$ = 95.2 J/mm^3).

After heat treatment, the cylinders were machined and polished (Fig. 1 (a)). Tensile tests were conducted at room temperature using an Instron® 4500 machine at 0.1 mm/s, with extension measured by a Fiedler® laser extensometer. Three samples per condition and three vertical specimens with non-optimized parameters (Section 2.3) were tested for comparison.

2.5. Thermal treatments

The cylinders manufactured with each of the selected build inclination were divided into six sets of 3 samples each and post-treated thermally following the experimental program provided in Fig. 3 together with the thermal treatment curves.

The double aging (DA) was carried out in the furnace at 720 °C for 8 h before reducing the temperature to 620 °C slowly over a time of 2 h and keeping this for another 8 h. Afterwards, the cylinders were cooled to room temperature by furnace cooling (FC).

In order to completely dissolve the Laves and δ phases and to obtain a more homogeneous microstructure, a heat treatment temperature of 1155 °C was chosen for a combined solution and homogenization

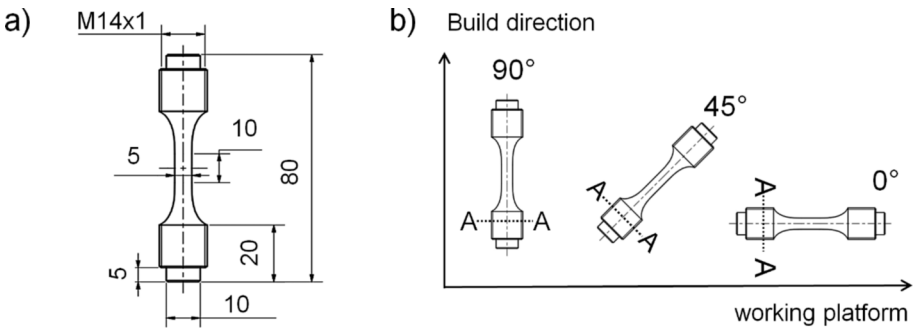

Fig. 2. Geometry of the round specimens for tensile testing (a), build direction at 0° (|| BD), 45° and 90° (⊥ BD) to the working platform (b), where "A-A" is the sectional location for the microstructural investigations and HEXRD analyses.

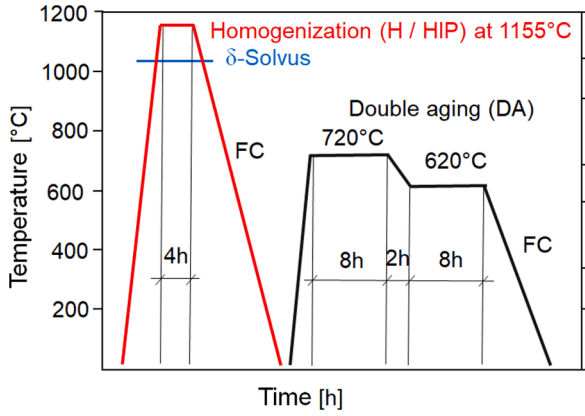

IN718	Treatment
AB	no (as built)
DA	double aged: 720 °C, 8h; ↘ to 620°C, 2h; 620 °C, 8h
H	heated: 1155 °C, 4h
H+DA	heated: 1155 °C, 4h; then aged by DA
HIP	heated: 1155 °C, 4h, 0.1 GPa, 4h
HIP+DA	heated: 1155 °C, 4h, 0.1 GPa, 4h; then aged by DA

Fig. 3. (a) Schematic representation of thermo(mechanical) treatments of LPBF IN718. (b) Different heat treatments studied in this experimental program. For each condition and build inclination, 3 specimens were tested.

annealing. The temperature exceeds the δ solvus temperature (reported in a range up to 1034 °C [38] by more than 100 °C. A third and fourth set of samples were H annealed in a furnace under an Ar atmosphere at 1155 °C for 4 h and then furnace cooled (FC) to room temperature. The cooling rate did not exceed 2 K/s. Half of the H samples (H + DA) were subjected to further double aging (DA) according to the scheme described above.

The remaining samples were subjected to hot isostatic pressing (HIP) at 1155 °C at 0.1 GPa for 4 h in an Ar atmosphere, followed by furnace cooling by Bodycote Ltd (Belgium). Half of them were also subsequently subjected to double aging (DA) – HIP + DA.

2.6. Microstructure, texture and phase analysis

Samples the different material conditions were prepared metallographically by cutting into parallel and perpendicular cross-sections and polished similar to those for the 2D porosity study (Section 2.3). For microstructure analyses a Helios Nanolab 600i FIB (Focused Ion Beam/Dual Beam, FIB/SEM) equipped with a circular backscatter (CBS) detector was used.

For energy dispersive X-ray spectroscopy (EDS), the Oxford ULTIM Max 100 detector was used on a Zeiss Ultra 55 Scanning Electron Microscope (SEM). An Oxford Nordlys II electron backscatter diffraction (EBSD) system was used on the same Zeiss SEM to determine the grain structure and to obtain texture information. The measurements were always carried out at the centre of the samples with significant distance to the edge.

Post-processing of the EBSD data was performed using the "HKL Channel5 software" (Oxford Instrument NanoAnalysis, version 5.12.62.0). Four measurements were carried out and the entire analyzed area per sample was ca. 2011 × 1494 μm^2. The reconstruction of the γ grains from the EBSD phase orientation maps and the calculation of the Schmid factor (SF) was performed using "HKL Tango" of HKL Channel5 software. The preferred grain orientation was determined by the corresponding EBSD inverse pole figures using the "HKL Mambo" (Crystal Orientation in Pole Figure) module. The Youngs modulus was calculated based on the acquired grain orientations using the software described in [60]. The elastic constants from Yang [61] were chosen for the calculation.

2.7. High-energy X-ray synchrotron diffraction analysis

The samples used for HEXRD characterization consisted of thin round plates of about 1 mm thickness and 10 mm diameter that were cut from the bottom of the cylindrical samples (Fig. 2).

High-energy synchrotron X-ray diffraction (HEXRD) was carried out at the beamline P07-HEMS of the PETRA III facility at Deutsches Elektronen-Synchrotron (DESY) Hamburg, Germany. An X-ray energy of ~ 100 keV (λ = 0.124 Å) was selected suitable to detect signals from small precipitates. IN718 powder and 8 LPBF samples of all 4 material states (i.e., AB, DA, HIP, HIP + DA) for longitudinal (parallel to the build direction: || BD) and transverse (⊥ BD) sections were examined.

In addition, for comparison of homogenized (H) and HIP treated samples were measured with ~ 73 keV (λ = 0.169 Å) at a large sample to detector distance to obtain a high angular resolution. For the X-ray diffraction analyses, the intensities of the Debye-Scherrer rings were first integrated along the azimuthal angle using Fit2D [62]. The diffractograms were evaluated with DIFFRAC.EVA V5.1 and DIFFRAC.TOPAS V5.0.

2.8. Deformation due to residual stresses

The residual stresses were evaluated on 110 mm long and 10 mm thick comb-shaped specimens comprising 26 thick tines (~1.7 mm) lined at the top with a 4-mm-thick bar (**Fig. S4 (a)**, Supplementary Materials). These comb-type specimens were built in different horizontal directions of 0°, 45° and 90° (**Fig. S4 (b))** with respect to the recoating and gas flow directions.

These specimens were cut from the build platform and their macroscopic deformation measured in order to qualitatively assess the magnitude of residual stresses in the material. The deformations were compared for AB samples manufactured with initial and optimized parameters and for DA samples manufactured with optimized parameters.

The vertical deformation of the specimens along their length ("actual" shape) were scanned with a GOM ATOS Q12 M (ZEISS®) optical measuring system on a rotating table GOM ROT 640 (Rev. 1.1), reconstructed three-dimensionally using the GOM Software 2021 and compared with the CAD model ("Target" shape). Alignment of the compared "actual" and "target" samples was performed out by fixing the left side. A more detailed illustration of the measuring scheme can be found in **Fig. S4 (c)** in the Supplementary Materials.

3. Results

3.1. Optimization of the LPBF bulk process parameters

The material densities varied significantly across the range of LPBF process parameters that was studied (Fig. 4). The optimization was conducted with a constant laser power of P = 180 W and varying the hatch distances and scan speeds, giving volume energy values E_V from 30 to 300 J/mm^3. This laser power is 10 % below the maximum nominal output of 200 W and was chosen to maintain process stability over time, accounting for potential performance degradation of the laser source, while enabling higher scan speeds and productivity. A layer thickness of t = 30 μm was selected to enable the future manufacturing of small cooling structures with high geometric accuracy. In general, the porosities obtained from the Archimedes measurements were slightly lower than those obtained from 2D image analysis. Nonetheless both methods showed good agreement in general trends (see **Fig. S2** (a-d) in the Supplementary Materials).

The dependence of porosity on the process parameters displayed a minimum at E_V = 60 J/mm^3, which was present with differently narrow regions for all studied hatch distances (Fig. 4 (a), blue marking). The minimum porosity for this set of parameters (P = 180 W, h = 100 μm and v = 1000 mm/s) was 0.32 % from the 2D-image analysis and 0.25 % from Archimedes measurements at a nominal IN718 density of 8.193 g/cm^3 (according to UNS N07718/W.Nr. 2.4668 [57]).

At energy densities below and above the optimum the porosity increases dramatically [14]. The contour diagram in Fig. 4 (b) illustrates the influence of hatch distance on material density within the E_V range of ~ 30 to ~ 100 J/mm^3. Notably, at hatch distances below approximately 60 μm, porosity is consistently very low and shows a minimal dependence on scanning velocity. This indicates the existence of a more robust processing window (the dark blue contour region at the left in Fig. 4 (b) and the orange curve in Fig. 4 (a)) than at the higher end of hatch values. However, small hatch distances can cause significant overheating of the boundary regions, leading to a distinct accumulation of defects in the contour regions, which were not considered in the quantitative analysis of the bulk porosity (see **Fig. S3** (f) in the Supplementary Materials).

In order to avoid possible boundary defects, the following set of parameters optimized for maximum material density was chosen for subsequent microstructure and heat treatment studies: velocity v = 1000 mm/s, hatch distance h = 100 μm, laser power P = 180 W, and layer thickness t = 30 μm, corresponding to $E_{V,opt}$ = 60 J/mm^3 (from the right dark blue area of Fig. 4 (b)).

The shape of the pores is influenced by various defect formation mechanisms [14,21,63,64]. Circular "keyhole" pores typically result from gas or vapor entrapment within the molten metal due to substantial overheating when E_V is significantly higher than the optimal $E_{V,opt}$ (deep welding regime; ascending right-hand side of the curves in Fig. 4 (a) with visualization in Supplementary **Fig. S3** (c)). Conversely, irregular slit-like "fusing defects" are caused by insufficient melting heat when E_V is much lower than optimal (ascending left side in Fig. 4 (a) and Supplementary **Fig. S3** (a)). With the optimized parameters (**Fig. S3** (b), the microstructure exhibits a minimal mixture of keyhole and fusing defect pores. These and other typical defects inherent in the residual porosity shown in **Fig. S3** (d – h) can only be further reduced by applying hot-isostatic pressing.

3.2. Microstructures and phase composition of the different LPBF IN718 material conditions

The microstructures of IN718 obtained by LPBF with the optimized parameters (v = 1000 mm/s, h = 100 μm, P = 180 W at t = 30 μm) are shown in Fig. 5 for four different post-treatment conditions:

- AB for cross-sections parallel and perpendicular to the build direction (BD) (Fig. 5 (a) and (b)),
- DA (Fig. 5 (c)),

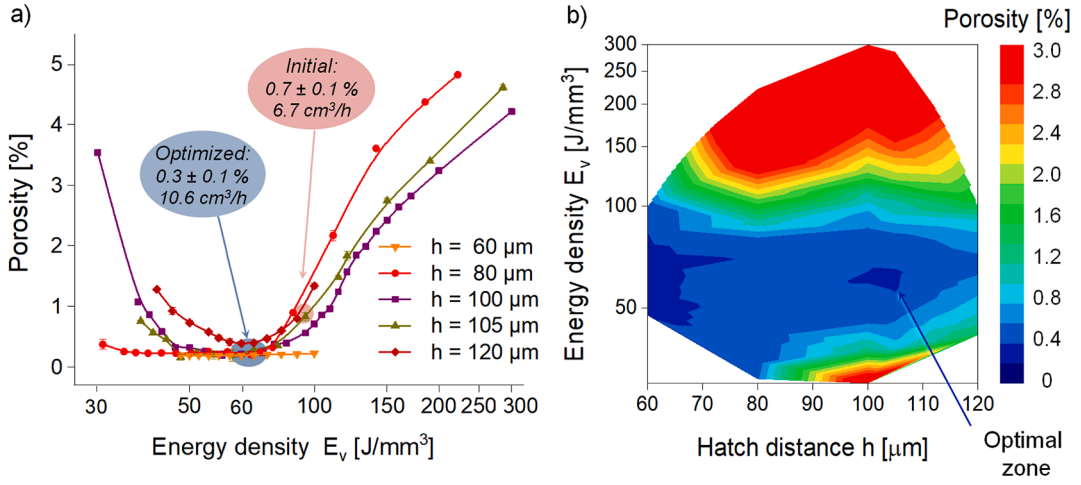

Fig. 4. The porosity of LPBF IN718 determined using the Archimedes method and plotted as a function of the energy density E_V (a) and for different hatch distances as a contour plot (b). The values shown are for a constant laser power of P = 180 W and a layer thickness of 30 μm.

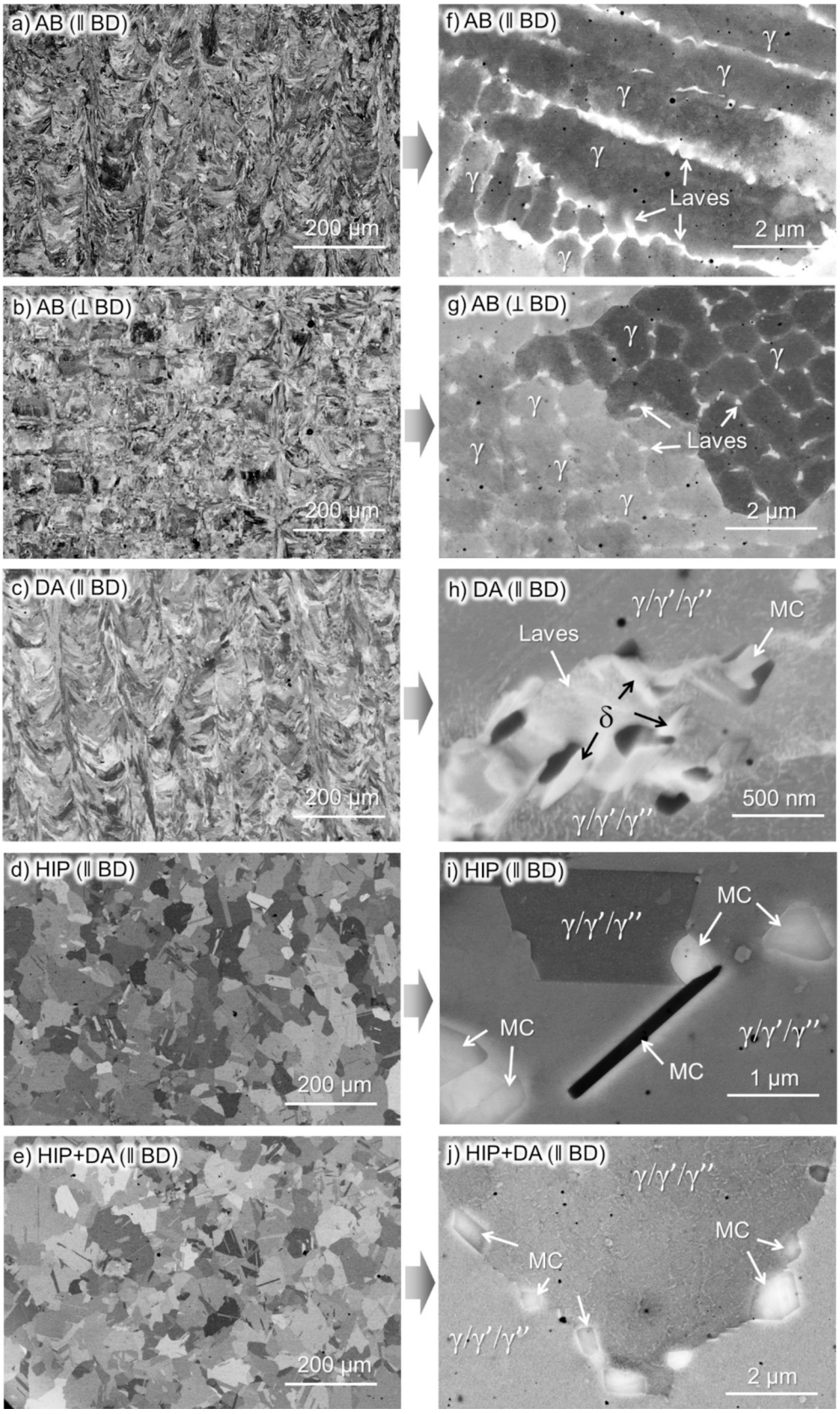

Fig. 5. Microstructures of the LPBF IN 718: as-built (∥ and ⊥ to the BD in (a, f) and (b, g), respectively), DA (∥ to BD, (c, h)), HIP (∥ to BD, (d, i)) and HIP + DA (∥ to BD, (e, j)) conditions. The figures on the right show detailed regions from the corresponding conditions on the left.

- HIP (Fig. 5 (d)), and
- HIP with a subsequent DA (HIP + DA; (Fig. 5 (e)).

The magnified images in Fig. 5 (f) to (j) of these conditions show the main phases, which have been assigned based on EDS (e.g., Fig. 6) as well as the HEXRD analysis (Fig. 7). The corresponding Debye-Scherrer rings from the HEXRD experiments are shown in Supplementary **Fig. S5**.

The LPBF IN718 **as-built microstructure** is characterized by a grain growth along the thermal gradient, resulting in the formation of dendritic γ grains framed by Laves phase at the interdendritic regions (Fig. 5 (a, f)). The grain structures remind of typical melt pool shapes known from other LPBF materials, albeit with the grains at the edges of the columnar patterns extending vertically along the build direction. In cross-sections perpendicular to the BD, the grains appear small and cellular (Fig. 5 (b,g)). The Laves phase is identified by HEXRD in both the initial LPBF powder feedstock and the AB material with phase fractions of approximately 2 wt% (Fig. 7 (a, b)). Both the powder and the AB material contain very small amounts of carbides (MC-type) according to HEXRD with phase fractions of ~ 0.2 wt% (Fig. 7 (a, b)). The amounts of Laves phase and carbides are in good agreement with the study of Čapek et al. [33]. However, in addition to the Laves phase and carbides, we identified no γ'' or further precipitates in the γ matrix.

The results of the EBSD analysis (Fig. 8 as well as **Fig. S6** and **Fig. S7** in the Supplementary Materials) are in line with a directional solidification of γ grains due to the heat flow. In the AB condition, a low area fraction of ~ 23 % shows a ⟨ 001⟩ orientation within 20° deviation in BD. The corresponding grains are mostly elongated and appear red in the analyzed section parallel (||) to BD Fig. 8 (a). These grains are supposed to correspond to the center of the melt pools. For the section orthogonal to BD (⊥, Fig. 8 (c)), a predominant ⟨ 001⟩ grain orientation in the scan directions is discernible: ~45 % of the area has ⟨ 001⟩ orientation within 20° deviation in scan direction In good agreement with the evaluation of the cross section parallel to BD, only ca. 26 % of the area has ⟨ 001⟩ orientation within 20° deviation in BD. Furthermore, the green colors of the inverse pole figure (IPF) map demonstrate that the majority of the grains (~40 % within 20° deviation) are oriented in the ⟨ 101⟩ direction along the BD (Supplementary **Fig. S6** (b)). This texture can be described as a weak to moderate Goss texture {101} ⟨ 001⟩ .

As the section parallel to the BD is cut at an angle of 45° to the scan direction (Fig. 9), the preferred ⟨ 001⟩ orientation in the scan direction was represented by choosing a reference direction of 45° between the x and z directions of the IPF map (Supplementary **Fig. S6** (a), XZ, β = 45°; ca. 40 % grain area with ⟨ 001⟩ orientation). This is consistent with the observation that numerous grains are depicted in blue colors, which corresponds to a < 111 > orientation in the IPF (X) and IPF (Z) maps shown in **Fig. S6** (a) and the pole figures in **Fig. S7** (a) in the

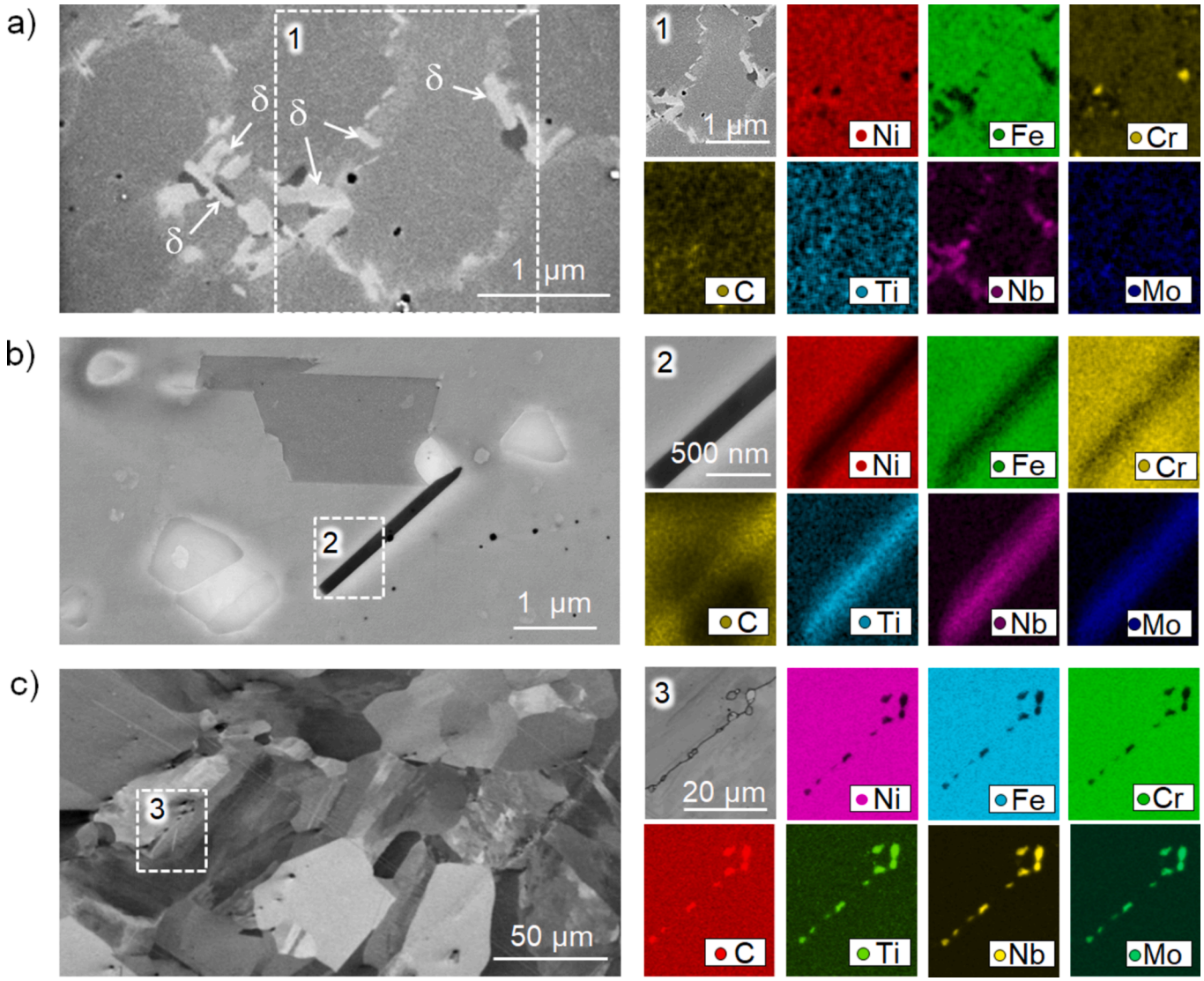

Fig. 6. Phase identification by EDS: δ phase in DA condition (a), needle-shaped (b) and equiaxed (c) carbides (Ti, Nb, Mo)C after HIP of an LPBF IN718 sample.

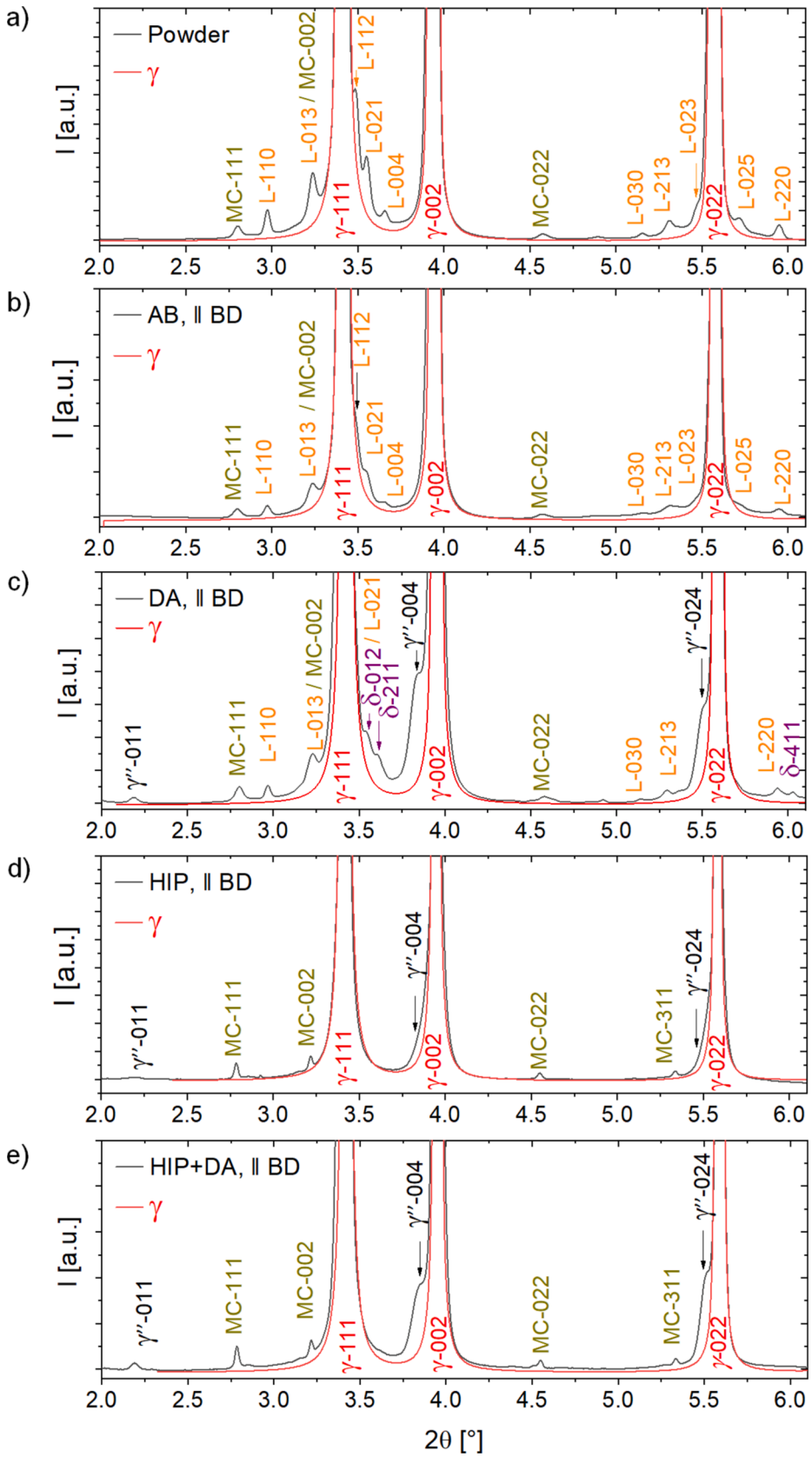

Fig. 7. Phase identification from HEXRD experiments for the IN718 powder (a), the LPBF IN718 AB (b) and the DA, HIP and HIP + DA heat-treated condition (c, d, e, respectively). The X-ray beam was oriented parallel to the BD of the samples. The corresponding Debye-Scherrer rings can be found in **Fig. S5** in the Supplementary Materials.

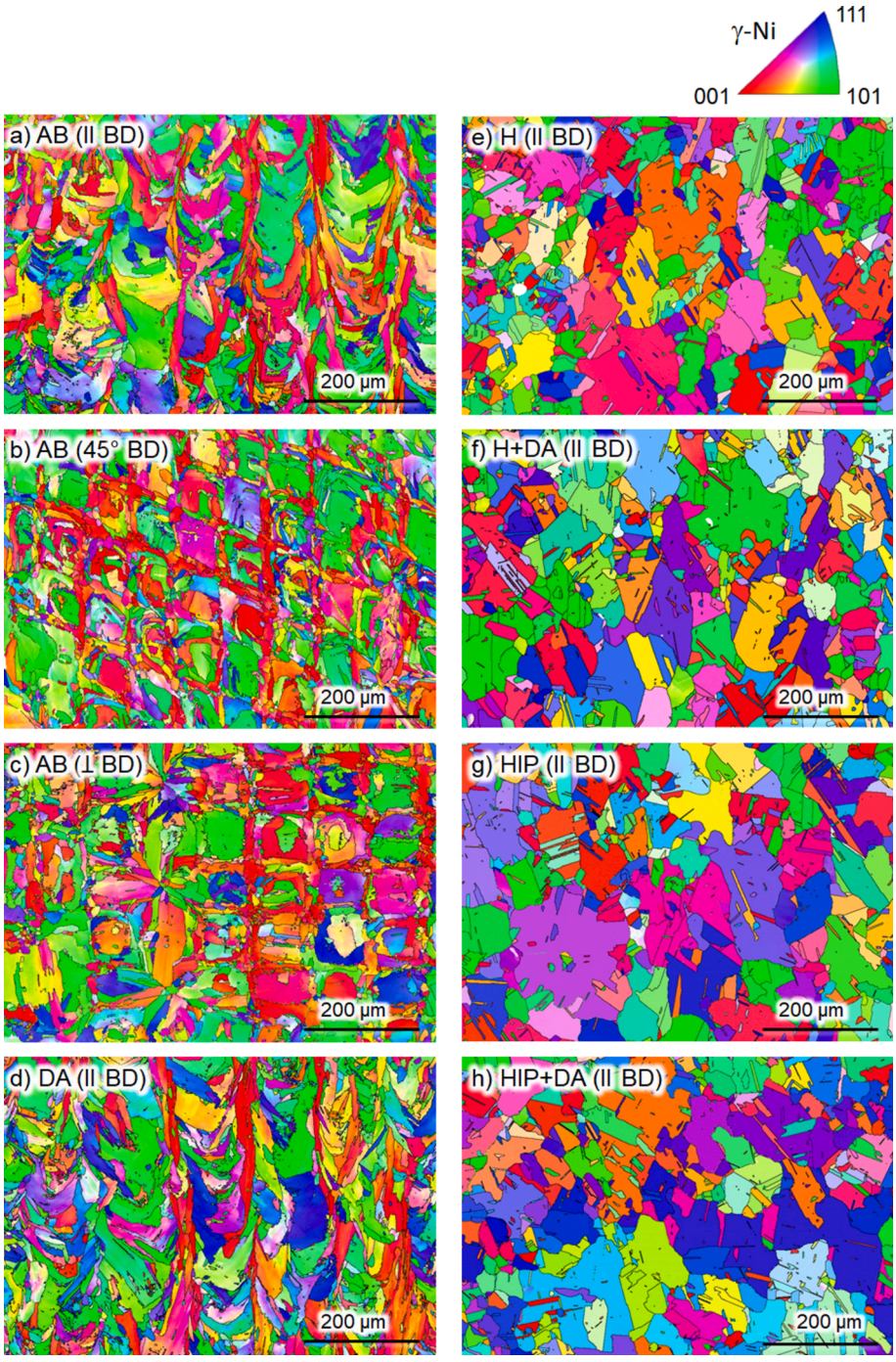

Fig. 8. Morphology and orientation of grains of the different LPBF IN718 states according to EBSD IPF maps: AB state (for orientations parallel (a, 90°) diagonal (b, 45°) and perpendicular (c, 0°) to the BD, and post-treated DA (d), H (e), H + DA (f), HIP (g) and HIP + DA (h) conditions for orientations parallel to the BD.

Supplementary Materials. The maximum of the multiple of uniform density (MUD_{max}) values for the IPF map (Y) of the perpendicular section is 4.2, while that for the IPF map (XZ) of the parallel section is 2.9 (**Fig. S6** (a, b)). The effect of the observed texture on the mechanical behavior will be discussed in Section 3.4.

The grain size analysis of the AB microstructure along the BD (∥) gives an average equivalent diameter of 13.4 µm compared to the orientation perpendicular to the BD (⊥) with an average diameter of 12.3 µm (Fig. 8, Fig. 8 and Table 2).

Overall the grain structure is rather fine, with more than 50 % of the grains having an equivalent diameter below 7.8 µm. The aspect ratios are computed from the grain morphology and are 3.1 and 2.5 for the parallel and perpendicular sections, respectively (Fig. 8 (e)).

The chosen DA temperature profile with holding levels at 720 °C and 620 °C was below the dissolution temperature of the metastable Laves phase (950 °C to ~ 1060 °C) [22–24] as well as below the temperature needed for recrystallization [35]. It did not cause grain coarsening and texture change compared to the AB state. The microstructure, analyzed by EBSD of a section along the BD is still fine-grained, with more than 50 % of the grains being smaller than 8 µm (Fig. 8 (g)), while the average grain diameter remained largely unaffected at 13.7 µm.

Larger alterations of the microstructure after the DA treatment are observed in the minor phases: The phase fraction of the Laves phase in the interdendritic regions has diminished in extent. The formation of

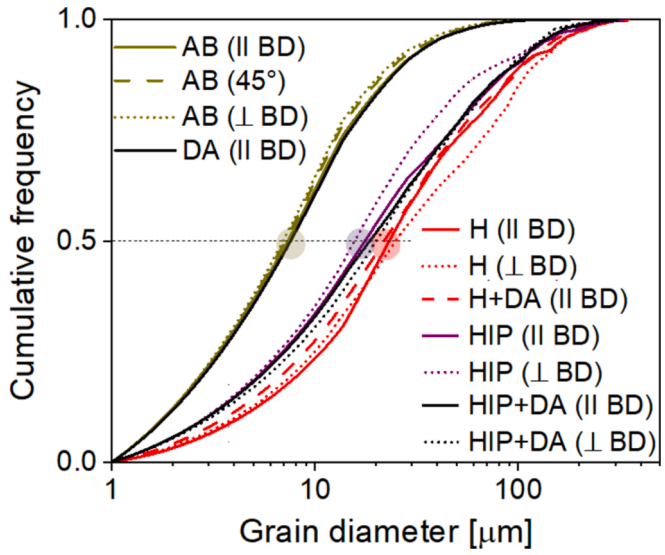

Fig. 9. Cumulative grain size analysis of the different LPBF IN718 states. The analyzed area of each sample is 2011 x 1494 μm^2.

Table 2
Comparative quantification of grains in different IN718 states (average values of analyzed surfaces of area 2011 x 1494 μm^2).

IN718 state	Maximum grain diameter [μm]	Average grain diameter [μm]	Average grain aspect ratio	50 % less than [μm]
AB (0°, ‖ BD)	215	13.4	2.78	7.8
AB (45° BD)	186	12.7	2.64	7.7
AB (90°, ⊥ BD)	137	12.3	2.46	7.6
DA (0°, ‖ BD)	158	13.7	2.99	7.9
H (0°, ‖ BD)	455	44.8	1.91	23.1
H (90°, ⊥ BD)	428	49.6	1.81	24.6
H + DA (0°, ‖ BD)	429	42.1	1.90	21.9
HIP (0°, ‖ BD)	333	38.2	1.89	17.7
HIP (90°, ⊥ BD)	270	32.5	1.95	15.8
HIP + DA (0°, ‖ BD)	529	37.5	1.83	18.4
HIP + DA (90°, ⊥ BD)	441	37.7	1.84	20.2

approximately 1 wt% of δ phase was confirmed by EDS (Fig. 6 (a)) and HEXRD (Fig. 7 (c)). The δ phase ($Ni_3(Nb,Ti)$) corresponds to the bright phase in the SEM image (Fig. 5 (h)). Thicker δ-plates were observed in the interdendritic regions, while thinner δ-needles formed within the interior of the γ matrix with different orientations (Fig. 5 (h)). The transformation of the Laves phase to δ during approximately 16 h of DA treatment, which has been previously reported in the literature [49,66,67] left only half of the Laves phase from AB (~1 wt according to HEXRD (Fig. 7 (c)).

The MC-type carbides (~0.2 wt%) were retained in the DA heat-treated material (Fig. 5 (c), and Fig. 7 (c)). Furthermore, after the DA treatment also the γ'' phase (Ni_3Nb, tetragonal, $D0_{22}$) was identified by HEXRD with a phase fraction of ~ 9 wt%.

However, it is important to note that γ' could not be distinguished in the diffraction and imaging data, although it is known from the literature to coexist with γ'' (see e.g. [33,37,52,65]). Consequently, we will henceforth refer to γ'/γ'' in our study.

The homogenization annealing (H), conducted at 1155 °C for a duration of four hours, resulted in a notable coarsening of the microstructure (Fig. 8 (g)). This observation was corroborated by the results of the HIP treatment, which exhibited a similar temperature–time profile. Consequently, only the image data pertaining to the HIP samples are presented, as they are also representative of the homogenized condition (Fig. 5 (d), Fig. 7 (d), Fig. 8 (d)).

Besides the coarsening, H or HIP at 1155 °C resulted in a substantial reduction of the AB texture. This transformation of the grain structure involved a transition to an equiaxed matrix with ca. 60 % Σ3 and ca. 5 % Σ9 grain boundaries. According to EBSD, the size for certain grains in the microsection along the BD was found to increase up to 300 μm in diameter with an average equivalent diameter of up to 38.2 μm for HIP vs. 44.8 μm for H (Fig. 8 (e)). This resulted in an average grain area of 2400 μm^2 (AB: 156 μm^2; Fig. 8 (a)). The texture exhibited a pronounced reduction as discussed below and the aspect ratio of the grains was found to be very similar: 1.96 versus 1.93 (averages from 2011 × 1494 μm^2 EBSD maps).

The brittle Laves phase was completely dissolved by H and HIP, and since the holding temperature exceeded the solvus temperature of δ [49,57] by more than 100 °C, the transformation of Laves to δ could be avoided. Only the γ matrix and MC-type carbides were observed in SEM images (Fig. 5 (d)). Moreover, the presence of small amounts of γ'' was inferred from HEXRD: the diffractogram shows slight shoulders at the left flanks of the γ-002 and γ-022 reflections of the γ phase (corresponding to γ''-004 and γ''-024, respectively), as well as the γ''-011 reflection (Fig. 7 (d), Supplementary **Fig. S5** (d)). The peaks of γ'' in the material after DA can be clearly recognized due to larger phase fraction and lattice mismatch (Fig. 7 (c) and (e); Supplementary **Fig. S5** (c) and (e)). The HEXRD images in Supplementary **Fig. S5** reveal the coherency of the γ'' phase with the γ matrix as the reflections appear at the same azimuthal angles.

After H and HIP, MC-type carbides are once again identified and EDS mappings suggest a composition (Nb, Ti, Mo)C (Fig. 6 (b) and (c)). Two main morphologies were identified through imaging techniques: equiaxial carbides, which were predominantly located along grain boundaries, and darker, needle-like carbides within the γ matrix.

Finally, an additional DA aging subsequent to H or HIP mainly affected the phase fraction of the γ'/γ'' phases as assigned from HEXRD (Fig. 7 (e)). Rather independent of the use of isostatic pressing, the microstructures of H + DA and HIP + DA exhibit a high degree of similarity. Therefore, only the HIP + DA samples are being presented. The SEM-CBS images demonstrate that the grain morphology of the longitudinal section of the sample resembles that of the HIP condition without additional DA (Fig. 5 (e)). This is evidenced by the presence of coarsened γ grains surrounded by carbides at the grain boundaries (Fig. 5 (h)). The results of the HEXRD analysis indicate a notable increase in the phase fraction of γ'' to approximately 8 wt% and a significant lattice mismatch between γ and γ'' (Fig. 7 (e)).

3.3. Distortion due to residual stresses

The magnitude of thermal residual stresses in the as-built state created by the thermal cycling and rapid cooling in the LPBF process was assessed qualitatively by measuring the macroscopic deformation of comb-type samples produced with either the initial parameters P = 180 W, v = 600 mm/s, h = 105 μm at t = 30 μm ($E_{v,in}$ = 95.2 J/mm3), or with optimized parameters P = 180 W, v = 1000 mm/s, h = 100 μm ($E_{v,opt}$ = 60 J/mm3).

The samples were removed from the working platform by wire spark erosion without prior thermal treatment. Furthermore, one set of samples produced with $E_{v,opt}$ was cut from the base plate after a heat treatment for stress reduction. For this purpose, the lower temperature DA treatment was selected. The sample arrangement on the working platform in the XY plane during printing was either parallel (0°),

diagonal (45°) or perpendicular (90°) to the coinciding directions of recoating and gas flow (Supplementary **Fig. S4 (b)**). Comparative measurements of the distortion of thin long sample combs along the length for the AB (initial), AB (optimized) and DA (optimized) can be found in Supplementary **Fig. S4 (e)-(g)**.

The different parameter sets lead to slightly different distortions. The deformations can be indirectly correlated to E_V as descriptor (albeit non-unambiguous) for the specific parameter sets. With the initial parameter set with $E_{v,in} = 95.2$ J/mm^3 deformations (Δ) of 8.80, 9.37 and 11.4 mm were obtained for the horizontal XY = 0°, 45° and 90° directions, respectively. The optimized parameters, corresponding to 60 J/mm^3, results in a reduction of the distortions to 8.61, 8.80 and 10.49 mm (XY = 0°, 45° and 90°), respectively. In stark contrast, the distortion was nearly reduced threefold by carrying out the DA annealing prior to wire arc erosion, with values of 3.2, 3.5 and 3.9 mm for XY = 0°, 45° and 90°, respectively.

The results are linked to the position and direction on the working platform due to the influence of the recoater movement and, most importantly, the direction of the Argon gas flow. Samples produced perpendicularly to the gas flow (90°) exhibited greater distortion than diagonally (45°) and especially parallelly (0°) built samples. The difference in displacement was up to 2.03 mm and 2.6 mm for the initial parameters and 1.69 mm and 1.88 mm for the optimized parameters.

Thus, the degree of distortion is strongly affected by the applied parameters and it decreased by 8 % with the parameter optimization (AB_{in} versus AB_{opt}). Even more significantly the stress relief annealing with the DA temperature profile reduced the distortions by ~ 60 % (AB_{opt} versus DA). Therefore, performing a stress relief annealing step prior to separation from the build platform should not be omitted even with a LPBF optimized scan strategy.

3.4. Mechanical strength

Firstly, the effect of optimising the LPBF process parameters on the mechanical performance of AB specimens fabricated with both initial and optimised parameters (Fig. 4 and **Section 3.1**) was evaluated by tensile tests (**Section 2.4**). The following mechanical properties were obtained for AB samples manufactured with initial $E_{v,in} = 95.2$ J/mm^3 at a 90° inclination to the working platform (average of the three samples): The yield strength (YS) was found to be 603 ± 34 MPa, while the ultimate tensile strength (UTS) was determined to be 942 ± 17 MPa. The Young's modulus (E) was measured to be 130 ± 26 GPa. The elongation at fracture (ε_f) was 31 ± 1.4 %.

Fig. 10 illustrates the notable improvement of strength and elongation at fracture relationships for LPBF IN718 samples produced with initial and optimised parameters in a vertical orientation (90°), in comparison to the properties of cast, wrought and wrought + DA alloys [57]. After parameter optimisation, the YS reached a value as high as 625 ± 8 MPa, while the UTS was enhanced to 1006 ± 3 MPa. Furthermore, Young's modulus (E) exhibited an increase to 195 ± 6 GPa. Finally, ε_f of the samples improved by up to 38 %.

In a second step, the trends in the mechanical performance were determined with the sets of specimens produced with optimized process parameters ($E_{v,opt}$ = 60J/mm^3) at inclinations of 0° (horizontal), 45° (diagonal) and 90° (vertical) to the build platform (Fig. 2). For the inclinations of 0° and 45°, only one orientation with respect to the recoater direction (or respectively, the argon flow direction) in the XY plane was considered. The measured yield strength (YS, (a)) and ultimate tensile strength (UTS, (b)) results are presented in Fig. 11 and will be discussed in Section 4.2. The numerical values of YS, UTS, E, and ε_f averaged over the three tests as well as their mean values within all investigated orientations at 0°, 45° and 90° are given in **Table S1** in the Supplementary Materials.

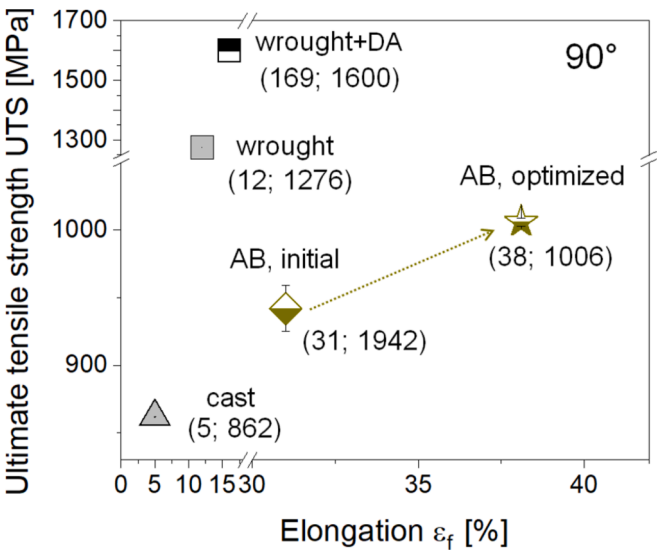

Fig. 10. Effect of optimizing LPBF process parameters on the strength and elongation at fracture for LPBF IN718 compared to reference materials. The values displayed in parentheses are the corresponding values of ε_f and UTS, respectively. The data for the LPBF material was obtained by averaging three measurements, while the data for the reference materials was sourced from [57].

4. Discussion

4.1. Process parameter optimization and porosity analysis

The optimisation of the LPBF process parameters for the bulk samples (Section 3.1) enabled an increase in material density from an initial 99.3 % to 99.7 % (Fig. 4) while simultaneously increasing productivity by nearly 60 %: the build rate was increased from 6.7 cm^3/h to 10.6 cm^3/h. The initial fractional porosity inherent in the IN717 powder used is partly responsible for the residual porosity of the samples even after careful process optimization (s. SEM image of a cross section of one of the particles in Fig. 1 (c)). A significant contributing factor to this productivity enhancement was the elevated scan speed of 1000 mm/s (compared to 600 mm/s initially), while the hatch distance remained close to the original value. The laser power and layer thickness were maintained at their initial settings as detailed in Section 3.1.

The volumetric energy density E_v calculated from each parameter set was employed as a simple indicator to facilitate comparisons between distinct parameters, which is valid when the parameters don't vary strongly. Importantly, E_V is not an unambiguous descriptor since, for example, doubling the hatch distance and halving the scan velocity provides the same E_V but not the same material quality (in worst case, to unconnected melt tracks can be achieved). The influence of individual parameters on porosity, as measured by both Archimedes and 2D techniques, is detailed in **Fig. S2** (a-d) in the Supplementary Materials.

While the absolute values from the Archimedes and the imaging analysis of porosity differ, the trends remain consistent. The optimized volume parameters correspond to $E_{v,opt}$ = 60 J/mm^3, which is significantly lower than the initial standard of 95.2 J/mm^3. The types of bulk defects detected in the LPBF as-built samples (**Fig. S3** in the Supplementary Materials) vary as a function of E_V during processing. As expected, the presence of lack of fusion pores at low E_V < ~40 J/mm^3 (Fig. S3 (a)) and keyhole pores at high E_V > ~100 J/mm^3 (**Fig. S3** (c)) is noted. The number of defects of both types increases in proportion to the difference between the optimal and applied laser energy densities as reflected by the left and right sides of the "energy density – porosity" curves (Fig. 4 (a) and (b)) and Supplementary **Fig. S2** (a)). These E_V threshold values vary slightly with the hatch distance used.

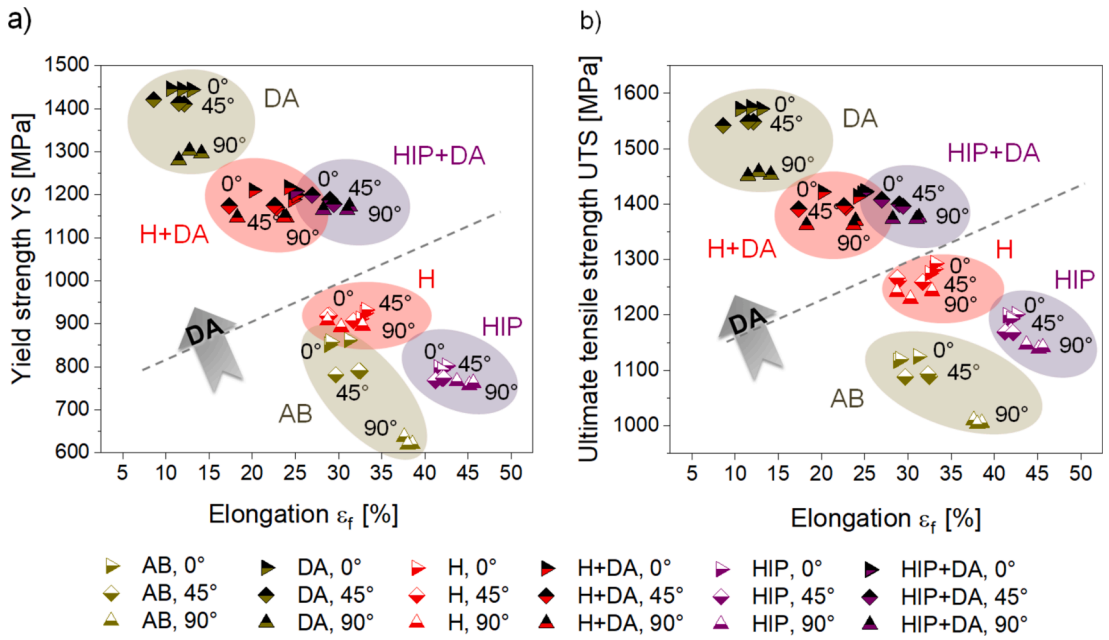

Fig. 11. The yield strength (YS, (a)) and ultimate tensile strength (UTS, (b)) as a function of elongation at fracture (ε_f) of LPBF IN718 with optimized parameters $E_{V,opt} = 60$ J/mm^3 for both as built and thermomechanical treated states for the different vertical build orientations of the specimens (0°, 45° and 90°).

Comparing with other studies, the optimized parameter set of this work with its $E_{v,opt} = 60$ J/mm^3 falls within the range of the majority of reported volumetric energy densities. Ignoring extreme E_V values in the literature, such as 41 J/mm^3 (Sufiiarov et al. [19]) at the lower end and 123.5 J/mm^3 (Ni and co-workers [28] and 145 J/mm^3 (Chlebus et al. [43]) at the upper end, the vast majority of reported parameters, range from approximately 50 to 90J/mm^3 (56.9 J/mm^3 by Hovig et al. [48], 57.7 J/mm^3 by Yao et al. [44], 59.4 and 59.5 J/mm^3 (for two sets with P = 250 and 950 W) by Popovich et al. [34], 61.7J/mm^3 by Götelid et al. [36], 67 J/mm^3 by Deng et al. [39], 68.3 J/mm^3 by Sufiiarov et al. [19], 71 J/mm^3 by Kuo et al. [32], 78 J/mm^3 by Aydinöz et all. [35], from 56.9 to 92.8 J/mm^3 by Kantzos [21], 90.3 J/mm^3 by Caiazzo et al. [20], 90.9 J/mm^3 by Nguyen et al. [45] This general agreement is particularly noteworthy given the different machines, laser sources, and optics used, including SLM Solutions 250^{HL} ([35,36,44]), SLM Solutions 280^{HL} ([19,48]), Realiser II [43], Farsoon 271 M [28], Concept Laser M2 [45], EOSINT M270 [6], EOS M280 [39], EOS M290 [38] and EOS M400 [40].

In terms of absolute porosity, our material-density-optimized set $E_{V,opt} = 60$ J/mm^3 provided values of 0.32 ± 0.06 % and 0.25 ± 0.02 from 2D image analysis and Archimedes measurements, respectively. In previous investigations, Aydinöz et al. [35] indicated a porosity of LPBF IN718 of 0.1 % at $E_V = 78$J/mm^3 (from 2D analysis), similar to that of Chlebus et al. [43] of 0.2 % at 145 J/mm^3. Also, Popovich et al. [34] reported consistent results from 2D analysis of 0.11 % porosity at 59.4 J/mm^3 using a parameter set optimized around a selected laser power of 250 W as well as 0.27 % for a set developed around P = 950 W on a SLM Solutions 280^{HL} setup.

Although all values are in the same range, porosity values ought to be treated with care given the dependence on the measuring method and its systematic errors, which renders the determination of porosity challenging. The results of the Archimedes method and 2D analysis depend on experimental performance and specific disadvantages, such as analysis of only very small image areas, weighing samples with open porosity and cracks, pore clogging during sample preparation, and insufficient measurement statistics. In the present work, porosity was investigated with particular care. For the 2D method, values were averaged over three 10 mm^2 cross-sections scanned pointwise with a high resolution of ~ 7500 x 5650 pixels and joined together using stitching (Section 2.3 and Supplementary **Fig. S1**). As a remark, at such small residual porosities other factors such as e.g., the type and exact location of these defects or other inclusions and undesired precipitates can become more important for the mechanical performance, e.g. the crack initiation under fatigue loading.

Lastly, HIP that is typically used to further reduce residual porosity and defects such as hot cracks [17,34,36,46,51] showed a further reduction in residual porosity for samples fabricated with the optimized set of parameters. After HIP treatment at 1155 °C and 0.1 GPa for 4 h, porosity decreased from 0.32 % to 0.01 % according to the 2D analysis. Since the Archimedes analysis does not give very reliable results in such a small porosity range, this data is omitted. The reduction in porosity is similar in magnitude to that observed in [34] due to the HIP treatment with slightly different process parameters there (e.g., from 0.11 % and 0.27 % to 0.02 % and 0.06 % for P = 250 W and 950 W, respectively).

However, the porosity clearly increased with subsequent DA treatment (HIP + DA): on average to 0.03 %. An increase in the porosity of HIP samples after subsequent DA annealing was also observed by Deng et al.: the porosity of their samples after DA increased to 0.04 and 0.07 % after DA [39].

4.2. *Relation between heat treatments, microstructures and mechanical performance*

The results from the tensile tests of differently heat-treated specimens presented in Fig. 11 can be divided into two groups depending the use of double aging (DA). Both groups can be separated by the dashed line, splitting them according to yield strengths and ultimate tensile strengths either above or below 1100 MPa and 1300 MPa, respectively. The not DA treated conditions show higher ductilities, with a range of elongation at fracture ε_f values between approximately 30 % and 45 %, whereas the double-aged conditions fall into a range of ε_f values between 10 % and 25 %. It should be noted that the chosen sample geometry results in somewhat higher ε_f values than typically reported for pure tensile sample geometries according to ASTM E8/E8M-11. The results of strength tests for the optimized IN718 material in comparison with the literature data are shown in the summary diagrams in Fig. 16 and Fig. 17 for 0° and 90° respectively.Firstly, a slight improvement of the tensile properties was obtained already through the parameter optimization aiming for the highest material density: i.e. in the vertical 90° build

direction the average YS and UTS of the samples increased by ~ 22 MPa and 64 MPa along with an improvement of ε_f from 31 % to 38 % (Fig. 10). In the as-built **(AB) condition** UTS values (Fig. 11**;** 1119, 1090 and 1006 MPa for 0°, 45°, and 90°, respectively) and YS values (855, 787 and 625 MPa for 0°, 45° and 90°, respectively) were obtained with the new optimized parameters $E_{V,opt}$ that generally correspond well to those of previous studies. A detailed literature assessment provided typical ranges of 904 MPa [43] to 1033 MPa [36] for UTS (Fig. 17**)** and 580 MPa [35] to 738 MPa [36] for YS for the 90° samples.

Noteworthy is again a comparison to the study by Popovich et al. [34], who for their two optimized parameters sets around the laser powers 250 W and 950 W, obtained substantially different YS and UTS (531 and 866 MPa versus 668 and 1011 MPa; ε_f of 21 and 22 % (Fig. 17**)**) in the AB material. Moreover, these authors also found a strongly reduced E-modulus of 113 and 173 GPa, albeit on flat dog-bone shape tensile samples spark-eroded from upright built blocks. Both LPBF parameter sets essentially shared the same resulting E_V of 59.4 and 59.5 J/mm^3 (porosity 0.11 % and 0.27 %) and, thus, the authors concluded that a coarser-grained microstructure and texture for the 950 W process window, was responsible for the differences [34].

The UTS averaged over the three build orientations, 1072 ± 59 MPa, exceeds that of the cast reference material (862 MPa) but falls short of the properties of wrought material (1276 MPa) [57]. The ε_f values of 30 % (0°), 32 % (45°), and 38 % (90°) are slightly larger than most reported values, but this is largely related to the different specimen geometries in the studies. Compared to cast IN718 reference with an ε_f of 5 % and wrought material with 12 % [57], the LPBF optimized AB condition clearly provides much better ductility. For a comparison of the tensile strengths with the extensive literature data available, refer to Fig. 16 and Fig. 17, which will be discussed below.

Importantly, the changes in mechanical performance, specifically the strength-ductility ratio, exhibit considerable variation following the analyzed heat treatments. This variation correlates with alterations in the microstructure, as evidenced by the distinct trend of the average YS and UTS for the three build orientations (Fig. 12).

The **DA condition**, obtained by annealing at 720 °C (8 h) and 620 °C (8 h), results in much higher strengths (UTS ~ 525 MPa; YS ~ 1384 MPa) but lower elongation at fracture (ε_f of ca. 12 %; Fig. 12). The microstructure analysis (Fig. 5 (c) and (h)) and HEXRD (Fig. 7 (c)) showed that this two-step DA caused a partial transformation of the Laves phase into the brittle, needle-shaped δ phase and the hardening γ'/γ'' phase. Since the DA temperatures were below the recrystallization temperatures, the texture and grain size distributions remained largely unchanged from the AB condition (Fig. 8 (d) and (g)). This latter observation is in line with a study by Aydinöz et al. on the role of residual stresses and HIP for inducing recrystallization [35]. The significant increase in UTS and YS in the DA condition, can, thus, be traced back to the formation of coherent γ'/γ'' precipitates.

Besides the phases and microstructures, residual stresses and lattice defects such as dislocations have been reported to be crucial for changes in strength and ductility [39,41]. The formation of lattice defects is intrinsically linked to the high residual thermal stresses inherent to LPBF. The dislocation density is typically high in as-built LPBF materials like IN718 [39,41] due to the rapid solidification conditions. The internal energy stored in the lattice defects as well as the residual stresses is released upon annealing, although in the case of a low-temperature DA, the reduction in residual stresses was estimated by Deng et al. [39] at merely 2 % based on the Zener-Wert-Avrami function. The fraction of residual stresses $\sigma^{RS}/\sigma_0^{RS}$, where σ_0^{RS} is the initial residual stress, and σ^{RS} is the residual stress after thermal relaxation, decreases from 1 to 0.985 after DA, falls to 0.217 after S treatment (980 °C/1h), and reaches 0 after H (1080 °C/1h) [39]. However, the current results based on the deformation of the comb samples suggest a much more substantial reduction of residual stress by DA, albeit not entirely relieving them (Section 3.3 and Supplementary **Fig. S4** (f) versus (g)). The γ'/γ'' formation counteracts the reduction in residual stresses by the DA, leading to the overall strengthening.

The appearance of the δ phase primarily accounts for the loss of ductility compared to the as-built state, as also proposed by Idell et al. [66]. In their study, the presence of needle-shaped δ precipitates was found to pin the grain boundaries and impede grain growth and grain boundary sliding during annealing. Additionally, Calandri et al. found that dislocations tend to accumulate at interdendritic boundaries and secondary phases, particularly relatively large Laves particles, reducing ductility by blocking dislocation movement [24].

The **homogenization treatment (H)** as well as the **hot isostatic pressing (HIP)** at 1155 °C for 4 h were successfully employed to dissolve the Laves phase in the AB condition (and the δ phase forming from it upon annealing) simultaneously. The microstructures of H and HIP were observed to be very similar in this study (hence only HIP is shown in Fig. 5 (d) and (i)). This contrast reports by Aydinöz et al., who observed that the deformations caused by HIP led to recrystallization that pure solution annealing failed to induce [35]; however, the temperature of 1000 °C in that study was also substantially lower than the presently employed temperature. Moreover, having used an LPBF parameter set that showed a much higher scanning velocity than that in [35] which implies increased cooling rates, the current AB condition likely possessed a higher degree of lattice defects and residual stresses that also contribute to the driving force for recrystallization [68,69].

The SEM and EBSD analyses after H or HIP showed a substantial

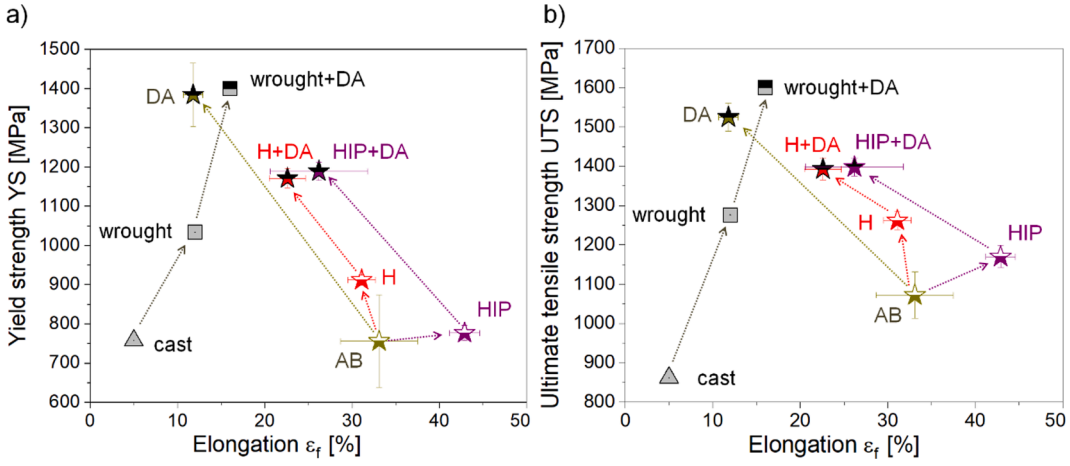

Fig. 12. Evolution of YS (a) and UTS (b) for different conditions of LPBF IN718 compared to the reference cast, wrought and wrought + DA materials. Average stress–strain values for the horizontal (0°), diagonal (45°) and vertical (90°) produced samples are presented.

recrystallisation: a much coarser grained microstructures with average diameters of approximately 48 μm and 36 μm, respectively, we observed compared to the initial AB condition or the DA material with values of approximately 12 μm to 13 μm (all averaged over microsections ∥ and ⊥ BD; frequency diagram Fig. 8 (g)). Doğu et al. [54] who starting with a microstructure that qualitatively resembles the microstructure from our study (Fig. 8 (a) and **Fig. S6** (a)) but exhibiting a cubic texture with a preferred ⟨ 001⟩ orientation in DB and in scan direction, demonstrated that annealing at 1050 °C for 45 min and 1150 °C for 15 min only slightly altered grain morphology and the texture. Annealing for 45 min at 1150 °C also caused a recrystallisation (for 79 % of the grains, which increased further to 92 % when the annealing temperature was raised to 1250 °C.

HEXRD ex situ analysis after HIP no longer showed the diffraction peaks of the Laves or δ phases that were clearly present in the AB or DA conditions (Fig. 7 (d) versus (a) – (c)). Together with the γ matrix, only the γ'/γ'' (Fig. 5 (i)) and MC carbide phases (Fig. 7 (d)) remained. The reflections of MC become sharper, which indicates a grain growth of the carbide particles. SEM and EDX revealed needle-like carbides within the matrix grains (Fig. 6 (b)) in addition to the spherical (Nb, Ti, Mo)C carbides at the grain boundaries (Fig. 6 (c)). The same observation is true for the H state of the LPBF material IN718.

Surprisingly, a comparative HEXRD analysis of H and HIP samples with finer angular resolution showed higher γ'' diffraction peaks in the H state compared to HIP that suggests higher contents of the γ'' strengthening phase (see peaks γ''-116, γ''-224, γ''-008 in Fig. 13). The exact amounts are much smaller than after DA and hence were difficult to quantify from HEXRD. The higher amount in the H condition can be understood from the slower cooling rate after H, whereas less time at elevated temperatures for transformation was available in the HIP treatment cycle.

The H condition exhibits lower strength compared to the DA material, with UTS values of ~ 1262 MPa and YS values of ~ 912 MPa, but presents sizable improvements by as much as ~ 190 MPa for UTS and 160 MPa for YS over the AB specimens (Fig. 11). The elongations at fracture, while higher than in the DA state, are comparable with the AB material at ~ 31 %.

Since the annealing at 1155 °C for 4 h fully relaxed the residual stresses, these no longer affect strength or ductility [39]. Therefore, we attribue the observed strength increases from the as-built (AB) state primarily to the formation of the γ'/γ'' precipitates. The absence of additional Laves and δ precipitates, which could impede dislocation and grain boundary movements, along with coarser grain sizes, explains the lower strength and values compared to the DA condition.

This aligns with findings from Hovig et al. [48] and Aydinöz et al. [35] where homogenization at 980 °C and 1000 °C resulted in UTS values of ~ 800 to ~ 1100 MPa and 870 MPa, respectively (s. Fig. 17). Although these values are lower, likely due to the lower homogenization temperatures leaving residual Laves or δ phases and producing less γ'', they showed a similar trend in strength evolution from the AB state.

The HIP condition in the current work exhibits lower strength compared to H (UTS ~ 1170 MPa and YS ~ 777 MPa) and, surprisingly, also the largest improvements in elongation at fracture from all conditions investigated in this work, reaching up to 43 %. Based on HEXRD this can be linked to the lower γ'' content in HIP versus H (Fig. 13) that occurs simultaneously with a smaller average grain size (which would act towards higher strengths) in the former microstructure (Fig. 8).

Götelid et al. [36] reported a UTS of ~ 1103 MPa (YS ≈ 723 MPa, ε_f ≈ 37 %) for vertically built samples after HIP treatment at 1150 °C and 0.15 GPa for 4 h. Despite slightly lower values than those in the current study, likely due to inclusions such as TiN found in fracture surfaces, the trends are consistent. Amato et al. achieved a comparable UTS of ~ 1140 MPa at slightly lower elongation at fracture (~30 %) after HIP at 1163 °C, preceded by solution annealing at 982 °C [46]. Popovich et al. [34] reported slightly lower strengths (UTS ≈ 1025 MPa, YS ≈ 645 MPa, εf ≈ 38 %) after HIP at 1180 °C (0.15 GPa, 3 h) on vertically built flat tensile specimens (s. Fig. 17).

Aydinöz et al. [35] observed a similar tensile property evolution from AB to H or HIP conditions using a HIP treatment at 1150 °C (0.1 GPa, 4 h) for vertically built samples. However, the absolute values differ due to the use of dog-bone shaped flat specimens. They proposed that the hydrostatic pressure during HIP, combined with the lattice deformations and residual stresses in AB material, leads to enhanced recrystallization compared to H treatment alone. This hypothesis is not confirmed by our EBSD analysis, which on the contrary shows significant recrystallization after H and HIP treatment. This isindicated by the reduced texture (maximum MUD-values of 2.2 and 2.3 for H and 2.6 and 3.4 for HIP for ∥ BD and ⊥ BD directions, respectively) compared to the as-built state (MUD values of 4.6 and 3.6, respectively) (Supplementary **Fig. S7**). In addition, the amount of CSL (coincident site lattice) boundaries is comparable for both conditions (H and HIP).

After a combined **HIP + DA and H + DA treatment,** the differences observed in the YS and UTS between the HIP and H routes largely disappear. The elongations at fracture remain slightly lower with ~ 23 % versus 27 % for the H + DA samples on average. Similar UTS (~1171 MPa vs. 1189 MPa) and YS (~1393 MPa vs. 1398 MPa) values are measured that can be understood from the similar γ'' fractions after DA in both conditions (grain sizes average grew closer with 42.1 vs. ~ 37.6

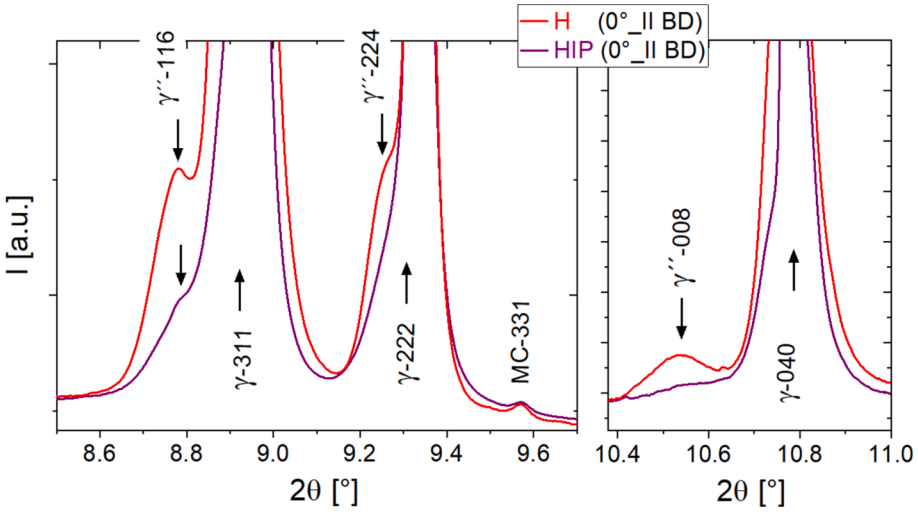

Fig. 13. Comparative HEXRD analysis for H and HIP. The X-ray beam was oriented parallel to the BD of the samples.

μm, Fig. 8). However, over the pure H and HIP states the added double-aging significantly increased UTS by ~ 130 MPa and ~ 220 MPa, respectively, at the cost of reduced ductility. The strengthening is attributed to increased γ'' phase fraction (evidenced by elevated γ''-011, γ''-004, and γ''-024 peaks, Fig. 7 (e) vs. Fig. 7 (d)), and the slight accumulation of coarsened MC-type carbides at grain boundaries, which may initiate cracks and reduce elongation values.

No additional secondary precipitates were identified in the investigated samples. Moreover, no γ'' dissolution with transformation into the δ phase as observed by Aydinöz et al. [54], did occur in the present case. SEM analysis of HIP + DA samples (Fig. 5 (e) and (j)) shows a microstructure similar to that of HIP-treated samples with coarsened MC-carbides at grain boundaries but no grain coarsening (average diameter ~ 37 μm; Fig. 8 (g)).

Other studies by Aydinöz et al. [35], Götelid et al. [36] and Popovich et al. [34] confirm similar trends for HIP + DA, with UTS increasing to 1315, 1371, and 1376 MPa (at P = 250 W), respectively, and ε_f dropping to 15 %, 14 %, and 15 %, respectively. Combined heat treatments without isostatic pressure (H + DA) yield comparable properties. Hovig et al. [58] reported improved UTS strengths (~1400 MPa) and reduced ductility (5–16 %) after double-aging following solution annealing at T ~ 980 °C. Strößner et al. [42] and Yao [44] found ε_f values of 17 % and 15 % (UTS ~ 1387 and 1409 MPa) after homogenization at 1065 °C and 1070 °C before DA. Deng et al. [39] achieved a UTS of ~ 1400 MPa with almost 25 % elongation after H + DA with additional solution annealing at 980 °C. Li et al. [41] reported increased εf of 24 % and a UTS of ~ 1325 MPa after H at 1165 °C followed by DA at 760 °C and 650 °C, attributing good plasticity to recrystallization and annealing twins, while γ' and γ'' precipitates retained strength. This agrees with the evolution of H + DA and HIP + DA properties observed in this work (Fig. 16 and Fig. 17**)**.

4.3. Analysis of the influence of texture

Texture is often considered a hindrance for part design and sizing because it can lead to anisotropy in mechanical properties, resulting in higher efforts and costs for components fabricated via LPBF. Therefore, characterizing the texture and its changes after heat treatments is essential for part designers. The texture is affected by the part geometry, build orientation, and support strategy due to directional heat dissipation to the massive build platform.

The texture of the as-built LPBF IN718 condition in our study observed by EBSD (Fig. 8) deviates from reports in the literature, where mostly a preferred ⟨ 001⟩ orientation in build direction is reported, e.g. [28], Li [41], Hovig [48], Mostafa [53], Doğu [54], Ghorbanpour [56], Chizari [69] and their co-authors. In our case, only a rather weak ⟨ 001⟩ orientation in BD is recognized (corresponding to elongated grains in the center of the melt tracks, whereas a stronger ⟨ 001⟩ texturing in the directions of the laser scan vectors in the build plane is visible in the pole figure projection in {001} direction obtained from the EBSD data (Supplementary **Fig. S7(c)**, projection {001}, MUD maxima in center versus corners). Thus, in our case we observed a preferred ⟨ 001⟩ orientation in the direction of the melt tracks and a weak preferred ⟨ 101⟩ orientation in build direction, which can be characterized as a weak to moderate Goss texture.

Particularly insightful is the comparison with a study by Gokcekaya et al., who demonstrated that varying the build parameters can lead to qualitatively different textures [55]. While a high laser power of 360 W and a high scan rate of 1400 mm/s resulted in a so called "single-crystal-like microstructure" with a strong preferred ⟨ 101⟩ orientation in build direction, slower scan rates (1000 mm/s) resulted in a "crystallographic lamellar microstructure" with elongated grains in the center of the melt pools that show a preferred ⟨ 001⟩ orientation besides the preferred ⟨ 101⟩ orientation at the sides of the melt track. The ⟨ 101⟩ texture in BD is explained by the solidification direction diagonally (with preferred ⟨ 001⟩ orientation) from both sides of the melt pools towards its center. In contrast, a lower laser power of 180 W (scan speed 1400 mm/s) resulted in a "polycrystalline-like microstructure", which resembles the microstructure structure in our study that has been built with P = 180 W and v = 1000 mm/s much closer. The fact that such a polycrystalline-like microstructure formed in our study at lower scan velocities may be explained by differing hatch and layer thicknesses as well as secondary process parameters.

The observed AB LPBF IN718 texture (Fig. 8) can be correlated with the material anisotropy in the strength, elastic and plastic properties (Fig. 11). In general, samples printed vertically (90°) have slightly lower strengths YS/UTS (0°) > YS/UTS (45°) > YS/UTS (90°), but higher elongations: ε_f (0°) < ε_f (45°) < ε_f (45°). As the ratio of the YS of vertically versus horizontally built samples (Table 3) shows, these differences are most pronounced for AB and DA conditions and are strongly reduced once the H or HIP treatment has been performed, i.e., once recrystallization has increased grain sizes and homogenized the texture (Fig. 8 and **Fig. S7**).

The texture links to the activation of glide systems for plastic deformation in specific crystallographic directions to release shear stresses caused by external loading. The slip systems capable of resolving the highest shear stress with respect to the external load direction have the highest *Schmid* factor. The *Schmid* factors for IN718 have previously been analyzed by Ni et al. [28] and Hovig et al. [48] For a strong ⟨ 001⟩ fibre texture along the build direction of tensile samples, the *Schmid* factors of the most relevant FCC slip system {111} < 110 > were calculated by Ni et al. [28] at approximately 0.47 and 0.32 for the vertical and horizontal orientations, respectively, explaining the higher yield stress these authors obtained for horizontally printed samples.

While qualitatively in line with the analysis by Ni et al. [28] the less pronounced texture in the ⟨ 001⟩ BD in the current AB induced us to evaluate the local *Schmid* factors from the EBSD data in assess the influence of the scan directions. The local *Schmid* factors were obtained as averages of 4 EBSD maps with a total surface area of 2011 × 1494 μm^2 (Fig. 14 (a)-(e)), averaged and correlated to the corresponding YS of the materials (Fig. 15 (a)). The average *Schmid* factors for the AB samples (Fig. 15 (a)) increases from 0.439 and 0.444 to 0.463, suggesting that the slip systems of the γ matrix in upright printed samples are indeed more easily activated compared to those in the flat-produced samples. This trend is qualitatively in line with the decreasing YS from 855 MPa to 787 MPa and 625 MPa and the concurrent improvement in ductility (Fig. 11 (a)), but the increase in *Schmid* factors alone appears comparably small in contrast to the large YS changes. A small amount of "hard" grains with a much lower *Schmid* factors than the average, for instance, could have a strong effect on the tensile properties. The amount of such oriented grains indeed decreases as the build orientation switches from horizontal (0°; Fig. 14 (a), microsection ∥ BD) to 45° and upright (90°; Fig. 14 (c), microsection ⊥ BD).

Additional influences contributing to the build direction dependence of the YS have been proposed by Deng et al. [39], who also measured much higher YS in horizontally (~780 MPa) than in vertically (~620 MPa) built samples. Since their AB LPBF IN718 material was found to be "relatively isotropic from a crystallographic point of view" according to EBSD, exhibiting a ⟨ 001⟩ texture in BD even weaker than in the current study (maximum MUD values of 1.85 and 1.79 for BD = 90° and 0°, respectively). Deng et al. attributed the differences in plastic properties between the different build direction of the AB condition primarily to residual stresses and dislocations from rapid solidification during processing rather than crystallographic orientation [39]. Similarly, these factors can contribute in case of the present AB material, given the

Table 3
Yield strength ratio of vertically (0°) and horizontally (90°) built orientation in LPBF IN718.

Heat treatment condition	AB	DA	H	H + DA	HIP	HIP + DA
$\sigma^V_{0.2}/\ \sigma^H_{0.2}$	0.73	0.89	0.97	0.96	0.95	0.96

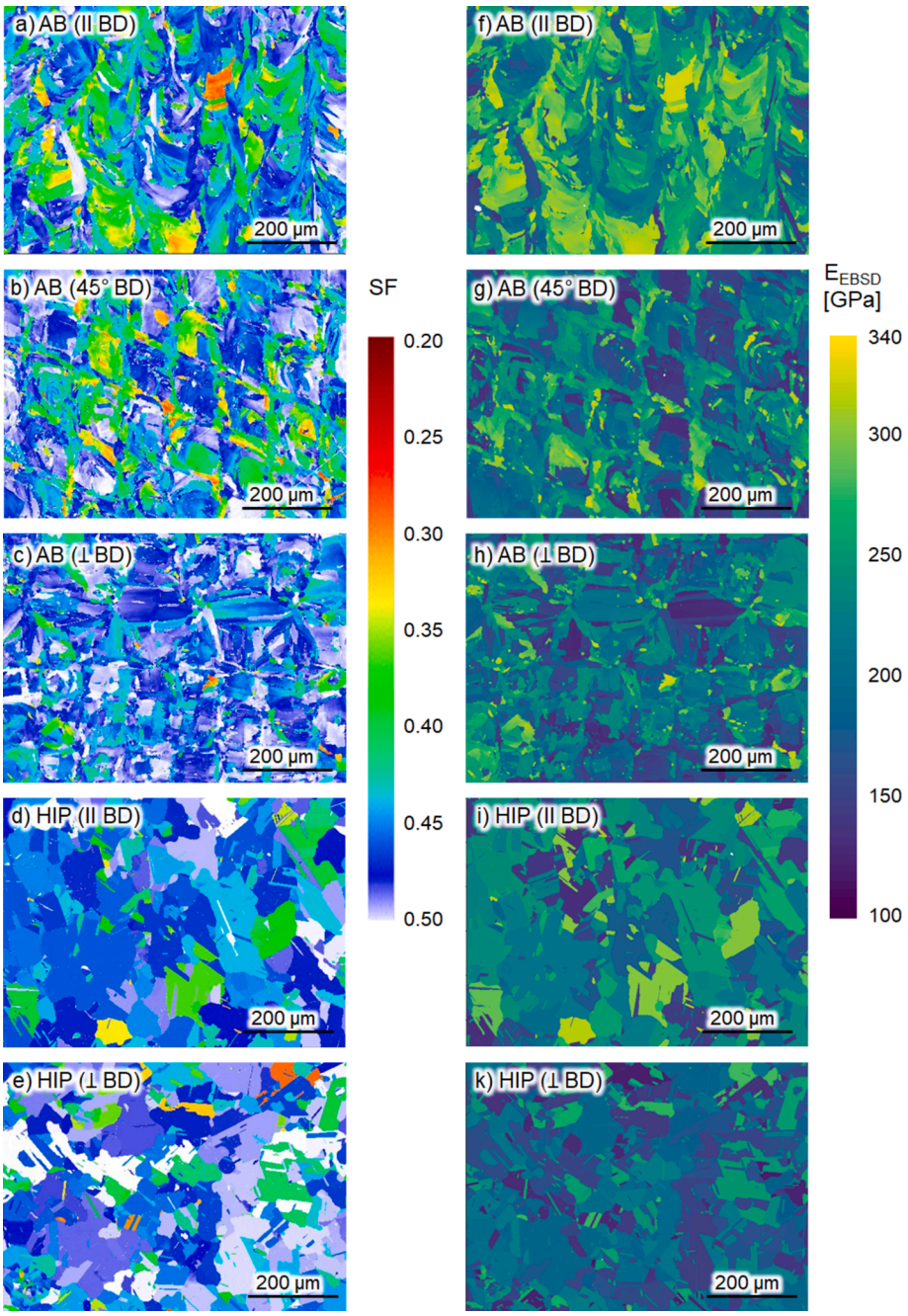

Fig. 14. Quantitative evaluation of the local Schmid factor (a-e, SF) and local distribution of effective Youngs modulus (f-k) calculated from EBSD data.

sizable distortion (Supplementary **Fig. S4 (b)**) implying high thermal residual stresses and the low texturing degree.

After HIP treatment, only small differences between the build orientations were found (Fig. 15 (a)). The YS (798 to 762 MPa for 0° and 90°) and the *Schmid* factors (0.455 and 0.459) were very close to each other. As already discussed EBSD analysis indicated a substantially reduced texture for H and HIP states and much coarser grains in contrast to the AB material. Thus, the recrystallized HIP- and H-treated samples behave quite "isotropically" in terms of mechanical properties and crystallography. This also holds true for conditions obtained with additional double-aging.

A comparison of the Young's modulus (E) derived from texture analysis from EBSD data and from the tensile tests (E_{exp}) shows that also the anisotropic elastic behaviour of the mechanical samples of the AB material can be traced back to the texture. Fig. 15 (b) shows the relation between E_{exp} and E_{EBSD} for the LPBF IN718 AB and HIP states of different building orientations. Average values of E_{EBSD} were calculated from the local values (Fig. 14 (f)-(k)) based on the elastic constant from [61].

The texture reduction from AB to HIP or H due to the treatments leads to a smaller spread in the Young's modulus values between the 0° and 90° build directions, i.e. also the elastic properties become more homogenized by the heat treatments in line with the more isotropic microstructure: from 217 GPa vs. 195 GPa in AB towards 203 GPa to 192 GPa after HIP (Fig. 14 (b) and **Table S1**). Youngs moduli for the upright built samples (90°) varied little with the heat treatment condition: 195 GPa (AB), 195 GPa (H) and 192 GPa (HIP). Thus, both evaluations of the plastic and elastic mechanical behavior from our study demonstrates that the texture is strongly reduced but not fully eliminated in the HIP and H conditions. This observation is in line with the trend that Popovich et al. found for the E-moduli of the specimen produced at P = 250 W

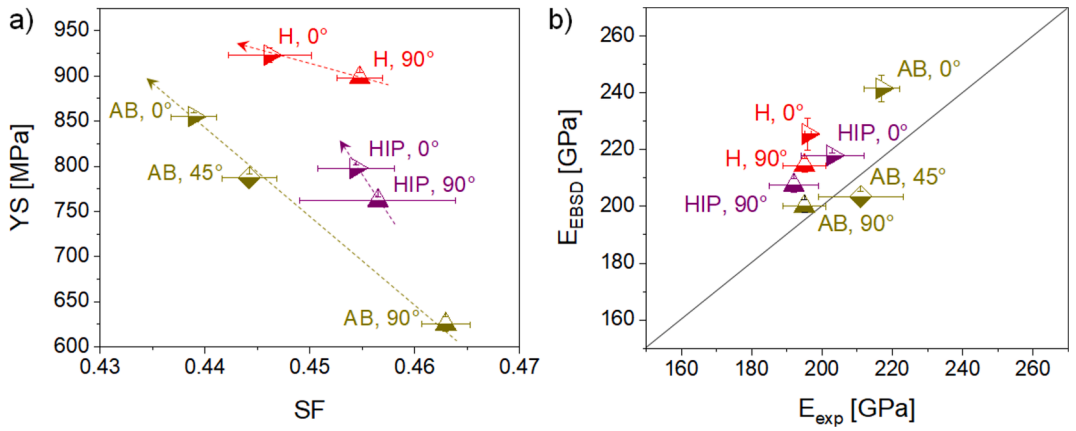

Fig. 15. Correlation of Yield strength (YS) and average Schmid factor (SF) calculated from EBSD measurements from 4 different areas (a). Correlation of calculated average Young's modulus (E_{EBSD}) based on elastic constants from [61] and measured E_{exp} from tensile tests (b) for the AB and HIP states of LPBF IN718.

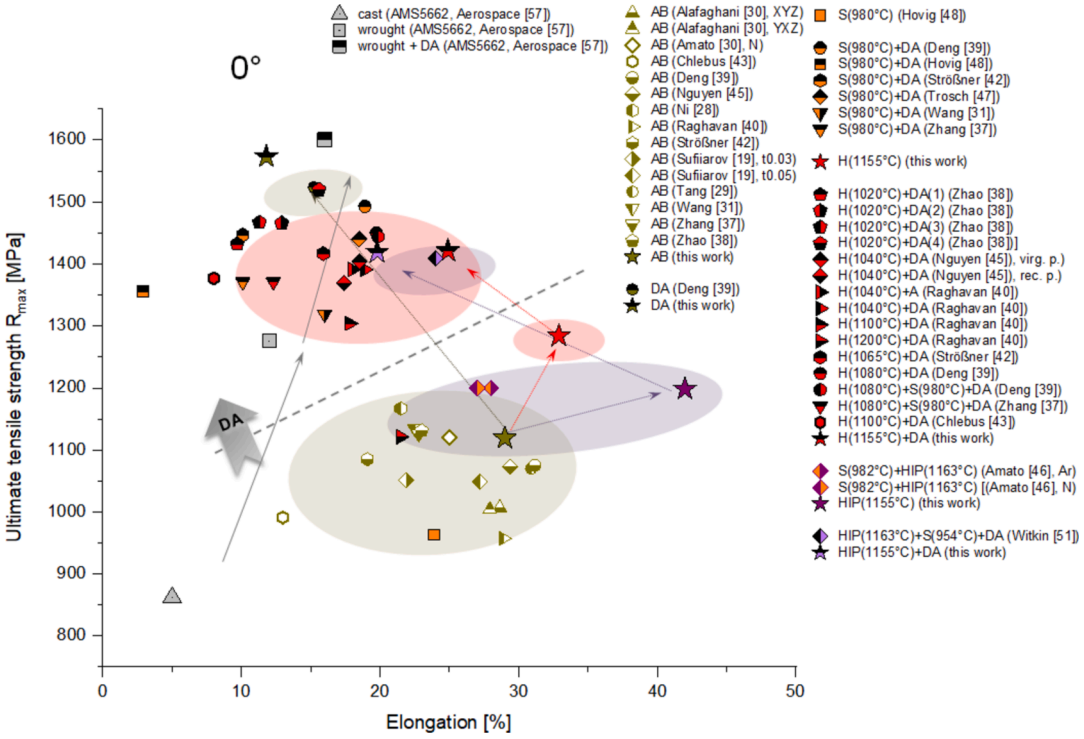

Fig. 16. Summary table of tensile behavior of AB and heat-treated LPBF IN718 for 0° build orientation.

power with a fine grained, polycrystalline material. For these specimens, the Youngs moduli also increased only slightly from 173 GPa in the AB state to around 180 to 190 GPa after HIP and HIP with aging [34].

The correlation between optimized LPBF parameters, microstructure, phase evolution, and mechanical properties offers valuable insights into the material performance. A comparative analysis with existing literature underscores the significant progress achieved in optimizing strength and ductility for critical applications. Future research will focus on assessing the fatigue properties of IN718 under cyclic loading, a crucial aspect for high-stress environments such as turbine blades with cooling channels, where cyclic performance directly impacts material reliability and lifespan. These investigations aim to deepen the understanding of the interaction between microstructure and cyclic loading behavior, paving the way for the development of advanced materials tailored to demanding applications.

5. Conclusions

This study provides new insights into the relationships between the microstructures, textures and anisotropic mechanical properties of LPBF processed Inconel 718 in as-built and heat-treated states. Moreover, by combining our experimental study with the vast amount of literature providing similar but also diverging results on this subject, commonalities and differences were identified.

1. Process window and Productivity: The process window optimization with respect to material density resulted in a parameter set corresponding to $E_{V,opt}$ = 60 J/mm^3 that showed almost 1/3rd higher productivity of 10.3 cm^3/h giving a porosity of 0.3 %. Importantly, wider margins of hatch and laser scan velocity values that only minimally increase porosity account for an increased robustness.
2. Effects of Double Ageing: DA at temperatures of 720 °C and 620 °C partially dissolves the Laves phase from AB initial state, precipitates

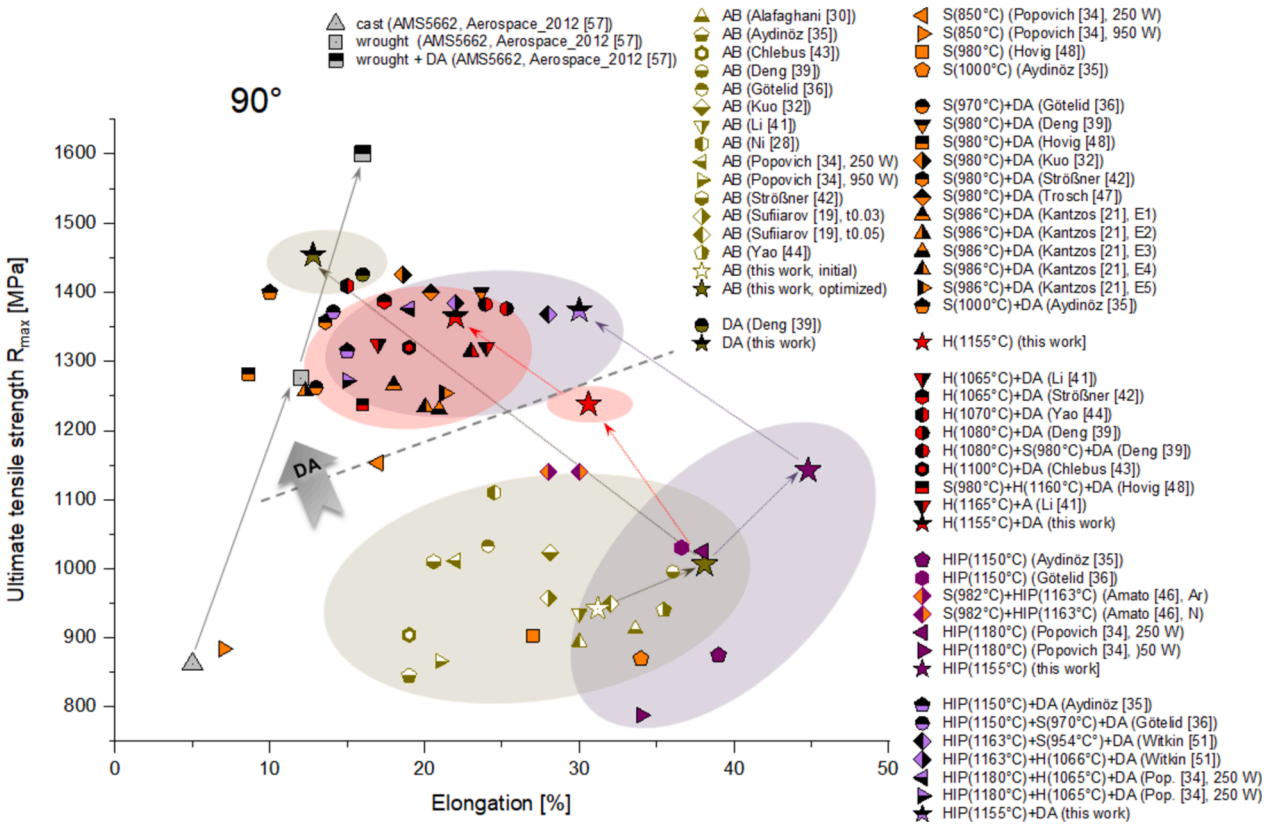

Fig. 17. Summary table of tensile behavior of AB and heat-treated LPBF IN718 for 90° build orientation.

the brittle δ as well as the strengthening γ'/γ'' phases, and promotes partial relief of residual stresses and dislocation recovery. This results in a significant strength increase with a corresponding decrease in ductility. No changes in grain size and texture were observed.

3. Effects of Homogenization and Hot Isostatic Pressing Treatments: H or HIP at 1155° dissolves the Laves and δ phases while also causing a substantial grain enlargement. Coarsened Carbides are found at the grain boundaries and as needle-like inclusions. Importantly, due to slower cooling a significantly higher amount of γ'' is detected in the H condition versus HIP by HEXRD. Consequently, H showed sizably increased strength over AB while not affecting ductility notably, whereas HIP improved the strength only slightly but resulted in the highest elongations of the investigated conditions.
4. Effects of subsequent DA after H or HIP: DA did not change the phase inventory qualitatively but lead to a quantitative increase in γ'' and carbides enlargement.
5. Anisotropy in Mechanical Properties and Texture evolution: Vertically built specimens loaded along the BD show lower strengths but higher ductilities, than horizontally printed ones (0°) loaded across the BD. Diagonally printed specimens (45°) behaved intermediate. The anisotropy of LPBF IN718 is related to texture where small differences in Schmid factors are obtained from EBSD analysis, but further influences from residual stresses and dislocations need to be taken into account to rationalize the large variations in mechanical properties. The texture and mechanical anisotropy are most pronounced in AB and DA and are more homogenized when a H and HIP treatment is added.
6. Relation between Texture and Scan Directions: Compared to the literature on LPBF IN718, the ⟨001⟩ texture in build direction in our material was less pronounced, but the material exhibited moderate preferred crystal orientations linked to the scan directions in the build plane (and weak ⟨101⟩ direction along the BD) i.e. a weak to moderate Goss-type texture. The scan strategy as well as specific laser parameters have a very strong influence on the texture evolution despite quantitatively the fairly similar E_V values.

In closing, we observe that substantially different process windows with comparable material densities can be obtained for this material that can differ strongly in properties such as productivity, robustness, or texture formation and mechanical properties. By correctly selecting proper heat treatment conditions, detrimental δ and Laves phases can be avoided the strength and ductility tuned in a sizable range, and texture and anisotropy largely eliminated.

CRediT authorship contribution statement

Galina Kasperovich: Writing – original draft, Visualization, Investigation, Formal analysis, Conceptualization. **Joachim Gussone:** Writing – review & editing, Validation, Methodology, Investigation, Formal analysis, Conceptualization. **Guillermo Requena:** Writing – review & editing, Project administration, Methodology, Funding acquisition, Data curation. **Norbert Schell:** Software, Methodology. **Andreas Stark:** Software, Methodology. **Jan Haubrich:** Writing – review & editing, Supervision, Project administration, Formal analysis, Data curation, Conceptualization.

Declaration of competing interest

The authors declare that they have no known competing financial interests or personal relationships that could have appeared to influence the work reported in this paper.

Acknowledgments

The authors would like to thank Mr. D. Birlo, Mr. T. Merzouk and Mr. A. Turak for their support with the LPBF machine preparation and

operation, the sample machining and the mechanical testing. C. Dresbach is acknowledged for providing the software EEDAS for the calculation of the local elastic properties and T. Strohmann and A. Klein for reprogramming the software to Python 3.

Appendix A. Supplementary data

Supplementary data to this article can be found online at https://doi.org/10.1016/j.matdes.2025.113627.

Data availability

Data will be made available on request.

References

[1] B.P. Conner, G.P. Manogharan, A.N. Martof, L.M. Rodomsky, C.M. Rodomsky, D. C. Jordan, J.W. Limperos, Making sense of 3-D printing: Creating a map of additive manufacturing products and services, Additive Manuf. 1–4 (2014) 64–76, https://doi.org/10.1016/j.addma.2014.08.005.
[2] P.R. Gradl, D.C. Tinker, J. Ivester, S.W. Skinner, T. Teasley, J.L. Bili, Geometric feature reproducibility for laser powder bed fusion (L-PBF) additive manufacturing with Inconel 718, Additive Manuf. 47 (102305) (2021) 1–33, https://doi.org/10.1016/j.addma.2021.102305.
[3] C.Y. Yap, C.K. Chua, Z.L. Dong, Z.H. Liu, D.Q. Zhang, L.E. Loh, S.L. Sing, Review of selective laser melting: materials and applications, Appl. Phys. Rev. 2 (2015) 041101, https://doi.org/10.1063/1.4935926.
[4] S. Singamneni, L.V. Yifan, A. Hewitt, R. Chalk, W. Thomas, D. Jordison, Additive manufacturing for the aircraft industry: a review, J Aeronaut Aerospace Eng 8, 1 (2019) 215, https://doi.org/10.35248/2168-9792.19.8.215.
[5] A. Uriondo, M. Esperon-Miguez, S. Perinpanayagam, The present and future of additive manufacturing in the aerospace sector: a review of important aspects. J Aerospace Eng (2015) 229(11), 2132– 2147, Doi: 10.1177/0954410014568797.
[6] F. Caiazzo, V. Alfieri, G. Corrado, P. Argenio, Laser powder-bed fusion of Inconel 718 to manufacture turbine blades, Int. J. Adv. Manuf. Technol. (2017) 93, 4023–4031 Doi: 10.1007/s00170-017-0839-3.
[7] G. Kasperovich, R. Becker, K. Artzt, P. Barriobero-Vila, G. Requena, J. Haubrich, The effect of build direction and geometric optimization in laser powder bed fusion of Inconel 718 structures with internal channels, Mat. Des. 207 (2021) 109858, https://doi.org/10.1016/j.matdes.2021.109858.
[8] A.J. Wildgoose, K.A. Thole, E. Tuneskog, L. Wang, Roughness related to cooling performance of channels made through additive manufacturing, J. Turbomach. 146 (5) (2024), https://doi.org/10.1115/1.4064310.
[9] G. Kasperovich, J. Hausmann, Improvement of fatigue resistance and ductility of selective laser molten TiAl6V4, J. Mat. Proc. Tech. 220 (2015) 202–214, https://doi.org/10.1016/j.jmatprotec.2015.01.025.
[10] S. Gialanella, A. Malandruccolo, Aerospace Alloys, Topics in Mining, Metallurgy and Materials Engineering (2020) Springer Nature Switzerland AG, Doi: 10.1007/978-3-030-24440-8.
[11] R.C. Reed, The superalloys: fundamentals and applications, Cambridge University Press, 31.07.2008, 1-392, Doi: 10.1017/CBO9780511541285.
[12] X. Wang, X. Gong, K. Chou, Review on powder-bed laser additive manufacturing of Inconel 718 parts, Proc IMechE Part B: J Engineering Manufacture (2016) 1–14, https://doi.org/10.1177/0954405415619883.
[13] T. Vilaro, C. Colin, J.D. Bartout, L. Nazé, M. Sennour, Microstructural and mechanical approaches of the selective laser melting process applied to a nickel-base superalloy, Mat. Sci. Eng. A 534 (2012) 446–451, https://doi.org/10.1016/j.msea.2011.11.092.
[14] G. Kasperovich, J. Haubrich, J. Gussone, G. Requena, Correlation between porosity and processing parameters in TiAl6V4 produced by selective laser melting, Mat. Des. 105 (2016) 160–170, https://doi.org/10.1016/j.matdes.2016.05.070.
[15] A. Sola, A. Nouri, Microstructural porosity in additive manufacturing: The formation and detection of pores in metal parts fabricated by powder bed fusion, J. Adv. Manuf. Proc. 10021 (2019), https://doi.org/10.1002/amp2.10021.
[16] M. Sadowski, L. Ladani, W. Brindley, J. Romano, Optimizing quality of additively manufactured Inconel 718 using powder bed laser melting process, Addit. Manuf. 11 (2016) 60–70, https://doi.org/10.1016/j.addma.2016.03.006.
[17] M. Valdez, C. Kozuch, E.J. Faierson, I. Jasiuk, Induced porosity in superalloy 718 through the laser additive manufacturing process: microstructure and mechanical properties, J. Alloys Compd. 725 (2017) 757–764, https://doi.org/10.1016/j.jallcom.2017.07.198.
[18] D. Wang, H. Han, B. Sa, K. Li, J. Yan, J. Zhang, J. Liu, Z. He, N. Wang, M Yan, A review and a statistical analysis of porosity in metals additively manufactured by laser powder bed fusion, Opto-Electron Adv. (2022) 5, No 10, Review, Doi: 10.29026/oea.2022.21005.
[19] V.S. Sufiiarov, A.A. Popovich, E.V. Borisov, I.A. Polozov, D.V. Masaylo, A.V. Orlov, The effect of layer thickness at selective laser melting, Procedia Eng. 174 (2017) 126–134, https://doi.org/10.1016/j.proeng.2017.01.179.
[20] F. Caiazzo, V. Alfieri, G. Casalino, On the relevance of volumetric energy density in the investigation of inconel 718 laser powder bed fusion, Materials (basel). 13 (3) (2020) 538, https://doi.org/10.3390/ma13030538.
[21] C. Kantzos, J. Pauza, R. Cunningham, S.P. Narra, J. Beuth, A. Rollett, An investigation of process parameter modifications on additively manufactured inconel 718 parts, JMEPEG 28 (2019) 620–626, https://doi.org/10.1007/s11665-018-3612-3.
[22] A. Niang, B. Viguier, J. Lacaze, Some features of anisothermal solid-state transformations in alloy 718, Mater. Charact 61 (2010) 525–534, https://doi.org/10.1016/j.matchar.2010.02.011.
[23] E. Bassini, G. Marchese, A. Aversa, Tailoring of the microstructure of laser powder bed fused inconel 718 using solution annealing and aging treatments, Metals 11 (2021) 921, https://doi.org/10.3390/met11060921.
[24] M. Calandri, S.Yin, B.Aldwell, F.Calignano, R. Lupoi, D. Ugues, Texture and microstructural features at different length scales in inconel 718 produced by selective laser melting, Materials (Basel) (2019) Apr.12(8),1293, Doi: 10.3390/ma12081293.
[25] F. Liu, F. Lyu, F. Liu, X. Lin, C. Huang, Laves phase control of inconel 718 superalloy fabricated by laser direct energy deposition via δ aging and solution treatment, J. Mater. Res Technol. 9 (5) (2020) 9753–9765, https://doi.org/10.1016/j.jmrt.2020.06.061.
[26] S. Sui, H. Tan, J. Chen, C. Zhong, Z. Li, W. Fan, A. Gasser, W. Huang, The influence of Laves phases on the room temperature tensile properties of Inconel 718 fabricated by powder feeding laser additive manufacturing, Acta Mater. 164 (2019) 413–427, https://doi.org/10.1016/j.actamat.2018.10.032.
[27] H. Xiao, S.M. Li, X. Han, J. Mazumder, L.J. Song, Laves phase control of Inconel 718 alloy using quasi-continuous-wave laser additive manufacturing, Mater. Des. 122 (2017) 330–339, https://doi.org/10.1016/j.matdes.2017.03.004.
[28] M. Ni, C. Chen, X. Wang, P. Wang, R. Li, X. Zhang, K. Zhou, Anisotropic tensile behavior of in situ precipitation strengthened Inconel 718 fabricated by additive manufacturing, Mater. Sci. Eng. A 701 (2017) 344–351, https://doi.org/10.1016/j.msea.2017.06.098.
[29] L. Tang, C. Wu, Z. Zhang, J. Shang, C. Yan, A lightweight structure redesign method based on selective laser melting, Metals 6 (2016) 280, https://doi.org/10.3390/met6110280.
[30] A. Alafaghani, A. Qattawi, M.A.G. Castañón, Effect of manufacturing parameters on the microstructure and mechanical properties of metal laser sintering parts of precipitate hardenable metals, Int. J.of Adv. Man. Techn. 99 (2018) 2491–2507, https://doi.org/10.1007/s00170-018-2586-5.
[31] Z. Wang, K. Guan, M. Gao, X. Li, X. Chen, X. Zeng, The microstructure and mechanical properties of deposited-IN718 by selective laser melting, J. of Alloys Compounds 513 (2012) 518–523, https://doi.org/10.1016/j.jallcom.2011.10.107.
[32] Y.L. Kuo, S. Horikawa, K. Kakehi, The effect of interdendritic δ phase on the mechanical properties of Alloy 718 built up by additive manufacturing, Mat. Des. 116 (2017) 411–418, https://doi.org/10.1016/j.matdes.2016.12.026.
[33] J. Čapek, E. Polatidis, M. Knapek, C. Lyphout, N. Casati, R. Pederson, M. Strobl, The effect of γ″ and δ phase precipitation on the mechanical properties of inconel 718 manufactured by selective laser melting: an In Situ neutron diffraction and acoustic emission study, JOM 73 (2021) 223–232, https://doi.org/10.1007/s11837-020-04463-3.
[34] V.A. Popovich, E.V. Borisov, A.A. Popovich, V.S. Sufiiarov, D.V. Masaylo, L. Alzina, Impact of heat treatment on mechanical behaviour of Inconel 718 processed with tailored microstructure by selective laser melting, Mat. Des. 131 (2017) 12–22, https://doi.org/10.1016/j.matdes.2017.05.065.
[35] M.E. Aydinöz, F. Brenne, M. Schaper, C. Schaak, W. Tillmann, J. Nellesen, T. Niendorf, On the microstructural and mechanical properties of post-treated additively manufactured Inconel 718 superalloy under quasi-static and cyclic loading, Mat. Sci. Eng. (2016) A 669, 246–258, Doi: 10.1016/j.msea.2016.05.089.
[36] S. Götelid, T. Ma, C. Lyphout, J. Vang, E. Stålnacke, J. Holmberg, S. Hosseini, A. Strondl, Effect of post-processing on microstructure and mechanical properties of Alloy 718 fabricated using powder bed fusion additive manufacturing processes, Rapid Prototyping J. 27 (9) (2021) 1617–1632, https://doi.org/10.1108/RPJ-12-2019-0310.
[37] D. Zhang, W. Niu, X. Cao, Z. Liu, Effect of standard heat treatment on the microstructure and mechanical properties of selective laser melting manufactured Inconel 718 superalloy, Mat. Sci. Eng. (2015) A 644 32–40, Doi: 10.1016/j.msea.2015.06.021.
[38] Y. Zhao, L. Hao, Q. Zhang, W. Xiong, Phase transformations during continuous cooling in inconel 718 alloys manufactured by laser powder bed fusion and suction casting, Mater. Charact. 185 (2022) 111764, https://doi.org/10.1016/j.matchar.2022.111764.
[39] D. Deng, R.L. Peng, H. Brodin, J. Moverare, Microstructure and mechanical properties of Inconel 718 produced by selective laser melting: sample orientation dependence and effects of post heat treatments, Mater. Sci. Eng. A 713 (2018) 294, https://doi.org/10.1016/j.msea.2017.12.043.
[40] S. Raghavan, B. Zhang, P. Wang, C.-N. Sun, M.L.S. Nai, T. Li, J. We, Effect of different heat treatments on the microstructure and mechanical properties in selective laser melted INCONEL 718 alloy, Mat. Manuf. Proc. (2016) 1–8, https://doi.org/10.1080/10426914.2016.1257805.
[41] X. Li, J.J. Shi, G.H. Cao, A.M. Russell, Z.J. Zhou, C.P. Li, G.F. Chen, Improved plasticity of Inconel 718 superalloy fabricated by selective laser melting through a novel heat treatment process, Mat. Design 180107915 (2019), https://doi.org/10.1016/j.matdes.2019.107915.
[42] J. Strößner, M. Terock, U. Glatzel, Mechanical and microstructural investigation of nickel-based superalloy IN718 manufactured by selective laser melting (SLM), Adv. Eng. Mater. 17 (8) (2015) 1099–1105, https://doi.org/10.1002/adem.201500158.
[43] E. Chlebus, K. Gruber, B. Kuźnicka, J. Kurzac, T. Kurzynowski, Effect of heat treatment on the microstructure and mechanical properties of Inconel 718

processed by selective laser melting, Mat. Sci. Eng. (2015) A 639, 647–655, Doi: 10.1016/j.msea.2015.05.035.
[44] X. Yao, S.K. Moon, B. Y. Lee, G.Bi, Effects of Heat Treatment on Microstructures and Tensile Properties of IN718/TiC Nanocomposite Fabricated by Selective Laser Melting, Int J. Precision Eng. Manuf. (2017), 18, 12, 1693-1701, Doi: 10.1007/s12541-017-0197-y.
[45] Q.B. Nguyen, M.L.S. Nai, Z. Zhu, C.N. Sun, J. Wei, W. Zhou, Characteristics of inconel powders for powder-bed additive manufacturing, Engineering 3 (2017) 695–700, https://doi.org/10.1016/J.ENG.2017.05.012.
[46] K.N. Amato, S.M. Gaytan, L.E. Murr, E. Martinez, P.W. Shindo, J. Hernandez, S. Collins, F. Medina, Microstructures and mechanical behavior of Inconel 718 fabricated by selective laser melting, Acta Mater. 60 (5) (2012) 2229–2239, https://doi.org/10.1016/j.actamat.2011.12.032.
[47] T. Trosch, J. Strößner, R. Völkl, U. Glatzel, Microstructure and mechanical properties of selective laser melted Inconel 718 compared to forging and casting, Mater. Lett. 164 (2016) 428–431, https://doi.org/10.1016/j.matlet.2015.10.136.
[48] E.W. Hovig, A.S. Azar, F. Grytten, K. Sørby, E. Andreassen, Determination of anisotropic mechanical properties for materials processed by laser powder bed fusion, Adv. Mater. Sci. Eng. (2018) Article ID 7650303, 1-20, Doi: 10.1155/2018/7650303.
[49] S. Azadian, L.Y. Wei, R. Warren, Delta phase precipitation in Inconel 718, Mater. Charact., (2004), 53, 1, 7-16, Doi: 10.1016/j.matchar.2004.07.004.
[50] X. Xie, C. Xu, G. Wang, J. Dong, W. Cao, R. Kennedy, TTT diagram of a newly developed nickel-base superalloy-Allvac® 718PlusTM, Superalloys 718, 625 and Derivatives (2005) 193–202. Doi: 10.7449/2005/superalloys_2005_193_202.
[51] D.B. Witkin, R.W. Hayes, T.D. Mclouth, G.E. Bean, Anomalous notch rupture behavior of nickel-based superalloy inconel 718 due to fabrication by additive manufacturing, Minerals, Metals Mater. Soc. ASM Int. 50A (2019) 3458–3465, https://doi.org/10.1007/s11661-019-05298-7.
[52] W.M. Tucho, P. Cuvillier, A. Sjolyst-Kverneland, V. Hansen, Microstructure and hardness studies of Inconel 718 manufactured by selective laser melting before and after solution heat treatment, Mater. Sci. Eng. A 689 (2017) 220–232, https://doi.org/10.1016/j.msea.2017.02.062.
[53] A. Mostafa, I.P. Rubio, V. Brailovski, M. Jahazi, M. Medraj, Structure, texture and phases in 3D printed IN718 alloy subjected to homogenization and HIP treatments, Metals 7 (2017) 196, https://doi.org/10.3390/met7060196.
[54] M.N. Doğu, K. Davut, M.A. Obeidi, M.A. Yalcın, H. Gu, T.S. E. Low, J. Ginn, D. Brabazon, Recrystallization and grain growth kinetics of IN718 manufactured by laser powder bed fusion (2022) J. Mat. Res. Technol., 19, 4242-4257, Doi: 10.1016/j.jmrt.2022.06.157.
[55] O. Gokcekayaa, T. Ishimotoa, S. Hibinoa, J. Yasutomi, T. Narushima, T. Nakano, Unique crystallographic texture formation in Inconel 718 by laser powder bed fusion and its effect on mechanical anisotropy, Acta Mater. 212 (2021) 116876, https://doi.org/10.1016/j.actamat.2021.11687.
[56] S. Ghorbanpour, K. Deshmukh, S. Sahu, T. Riemslag, E. Reinton, E. Borisov, A. Popovich, V. Bertolo, Q. Jiang, M.T.Sanchez, M. Knezevic, V. Popovich, Additive manufacturing of functionally graded inconel 718: Effect of heat treatment and building orientation on microstructure and fatigue behavior (2022) J. of Mat. Processing Tech. 306 117573, Doi: 10.1016/j.jmatprotec.2022.117573.
[57] S.A.E. Aerospace, Aerospace Material Specification: AMS 5662, SAE International, 2009, AMS5662: Nickel Alloy, Corrosion and Heat Resistant, Bars, Forgings, and Rings 52.5Ni 19Cr 3.0Mo 5.1Cb 0.90Ti 0.50Al 18Fe, Consumable Electrode or Vacuum Induction Melted 1775°F (968°C) Solution Heat Treated, Precipitation Hardenable - SAE International.
[58] ZEN SP1 (Black Edition)©, Carl Zeiss Microscopy GmbH, 2012 (1997-2013).
[59] AnalySIS©, Soft Imaging System GmbH, Muenster, Germany, 2002.
[60] C. Dresbach, U. Dressler, J. Gussone, S. Reh, Calculation of effective Young's modulus distribution from electron backscatter diffraction results for stochastic analyses in aerospace applications, Mater. Sci. Eng. Technol. 45 (2014) 5, https://doi.org/10.1002/mawe.201400235.
[61] S.W. Yang, Elastic constants of a monocrystalline nickel-base superalloy, Metall Trans. A 16 (1985) 661–665, https://doi.org/10.1007/BF02814240.
[62] A.P. Hammersley, FIT2D: a multi-purpose data reduction, analysis and visualization program, Doi: 10.1107/S1600576716000455.
[63] C. Zhao, N.D. Parab, X. Li, K. Fezzaa, W. Tan, A.D. Rollett, T. Sun, Critical instability at moving keyhole tip generates porosity in laser melting, Science 370 (2020) 1080–1086, https://doi.org/10.1126/science.abd1587.
[64] S. Sanchez, P. Smith, Z. Xu, G. Gaspard, C.J. Hyde, W.W. Wits, I.A. Ashcroft, H. Chen, A.T. Clare, Powder Bed Fusion of nickel-based superalloys: a review, Int. J. Machine Tools Manufact. 165 (2021) 103729, https://doi.org/10.1016/j.ijmachtools.2021.103729.
[65] L.-S.-B. Ling, Z. Yin, Z. Hu, J.-H. Liang, Z.-Y. Wang, J. Wang, B.D. Sun, Effects of the γ-Ni3Nb phase on mechanical properties of inconel 718 superalloys with different heat treatments, Materials 13 (2020) 151, https://doi.org/10.3390/ma13010151.
[66] Y. Idell, L.E. Levine, A.J. Allen, F. Zhang, C.E. Campbell, G.B. Olson, J. Gong, D. R. Snyder, H.Z. Deutchman, Unexpected δ-phase formation in additive-manufactured Ni-based superalloy, JOM 68 (2016) 950–959, https://doi.org/10.1007/s11837-015-1772-2.
[67] Y.L. Kuo, T. Nagahari, K. Kakehi, The effect of post-processes on the microstructure and creep properties of alloy718 built up by selective laser melting, Materials 11 (2018) 996, https://doi.org/10.3390/ma11060996.
[68] Z. Zhou, A.S. Gill, D. Qian, S. Mannava, K. Langer, Y. Wen, V.K. Vasudevan, A finite element study of thermal relaxation of residual stress in laser shock peened in718 superalloy (2011) Int. J. Impact Eng. 38 (2011) 590–596, Doi: 10.1016/j.ijimpeng.2011.02.006.
[69] A.M. Chizari, A. Kermanpur, E. Foroozmehr, A. Rezaeian, F. Sadeghi, A. Rezaei, Effect of solution treatment on microstructure and stress rupture properties of precipitation hardened IN718 superalloy fabricated by laser powder-bed fusion process, J. Mater. Res. Technol. 21 (2022) 2296–2308, https://doi.org/10.1016/j.jmrt.2022.10.047.

Supplementary Materials

Tailoring the Strength of Inconel 718: Insights into LPBF Parameters and Heat Treatment Synergy

Galina Kasperovich[(a)], Joachim Gussone[(a)], Guillermo Requena[(a,b)], Norbert Schell[(c)], Andreas Stark[(c)], Jan Haubrich[(a)]

a) German Aerospace Center (DLR), Institute of Materials Research, Linder Hoehe, 51147 Cologne, Germany
b) RWTH Aachen University, Metallic Structures and Materials Systems for Aerospace Engineering, 52062 Aachen, Germany
c) Helmholtz-Zentrum Hereon, Institute of Materials Physics, Max-Planck-Straße 1, 21502 Geesthacht, Germany

Section S1:

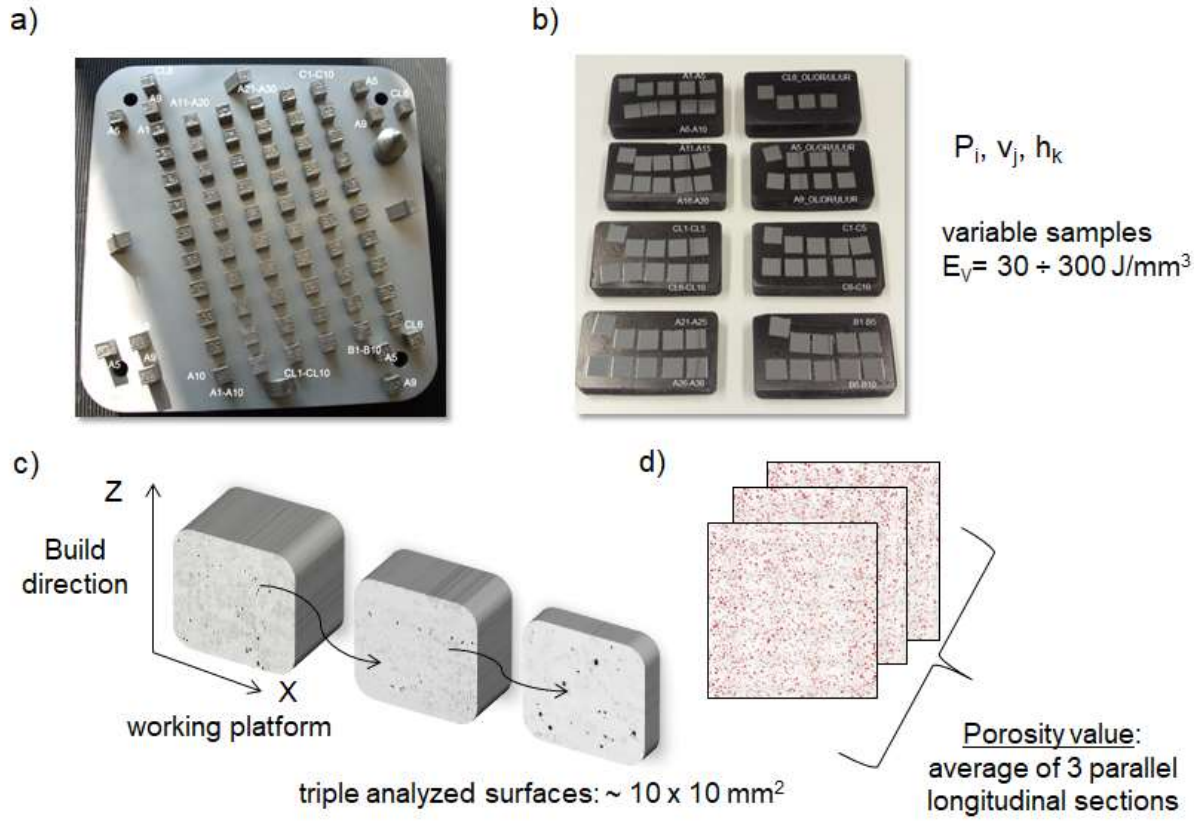

Fig. S1. 2D porosity analysis: samples produced with variation process parameters (a), preparations in blocks (b), longitudinal scanning scheme (c), analysis averaging (d).

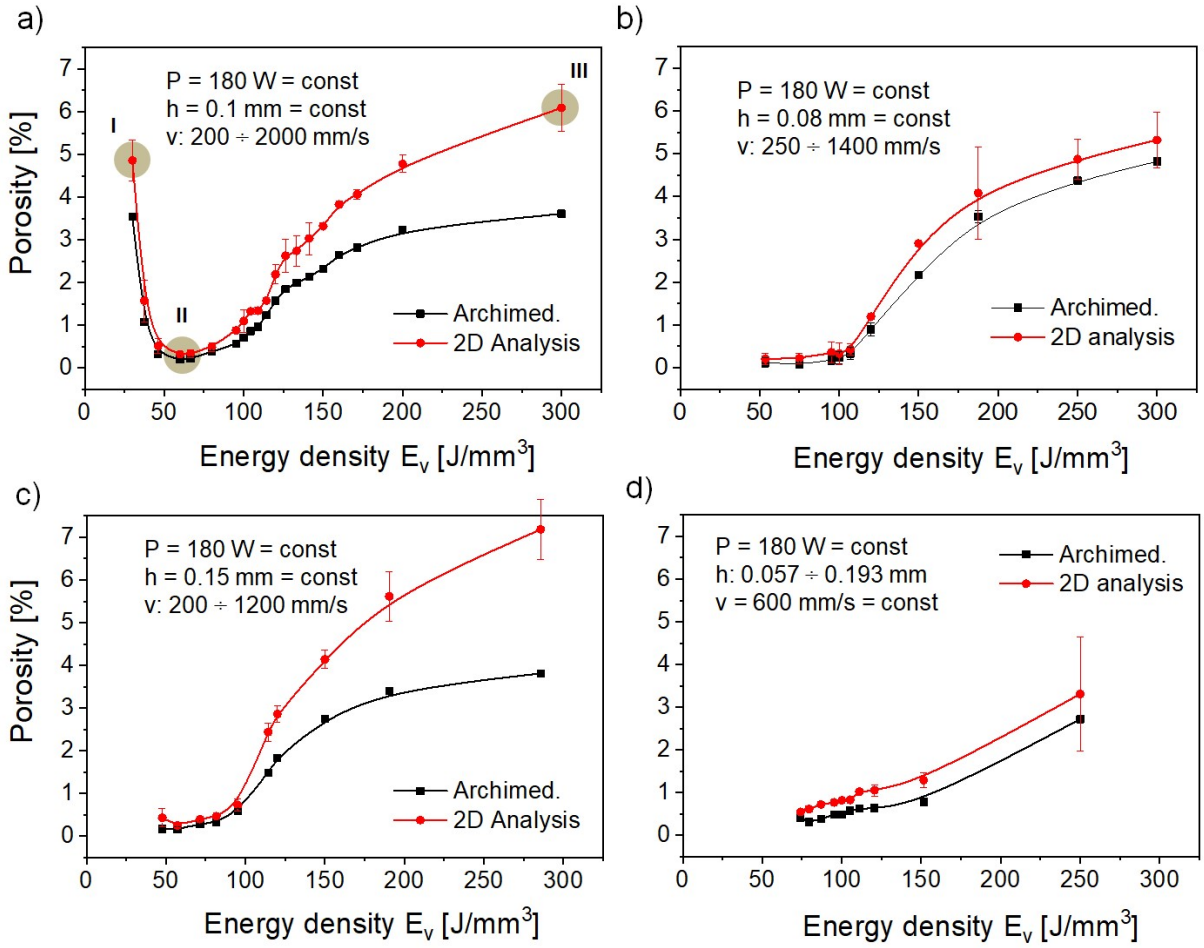

Fig. S2. Residual porosity of LPBF IN7128 measured by the Archimedes method and 2D image processing technique for a constant LPBF laser power of 180 W and hatch h = 0.1, 0.08 and 0.15 mm (a, b and c, respectively) and at varying hatch distances h for a constant velocity v of 600 mm/s (d). The areas of insufficient, optimal and excessive energy input into the material are labelled I, II and III and illustrated in **Fig. S3**.

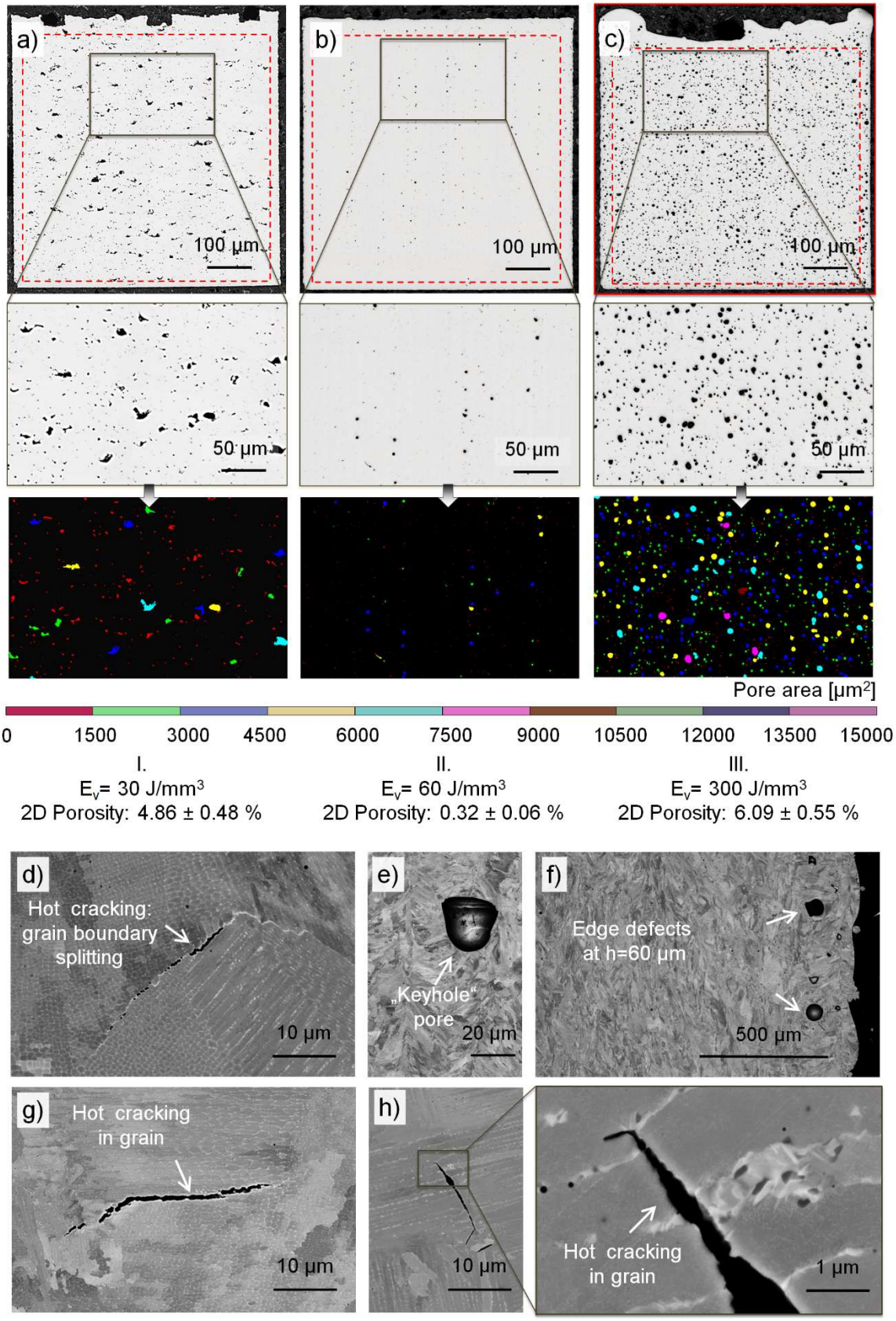

Fig. S3. Defect morphology as a function of the volume energy density E_V: IN718 produced with insufficient (a), optimized (b) and excessive (c) E_V and typical residual defects (d - h). The zones I, II and III correspond to those shown in **Fig. S2** (a). The analyzed area is ~ 1 mm², labeled with a red dashed square. Edge regions were not considered. Porosity values are averages of three measured sections. The colored scale under (a-c) is the classification of pores according to their area.

Section S2:

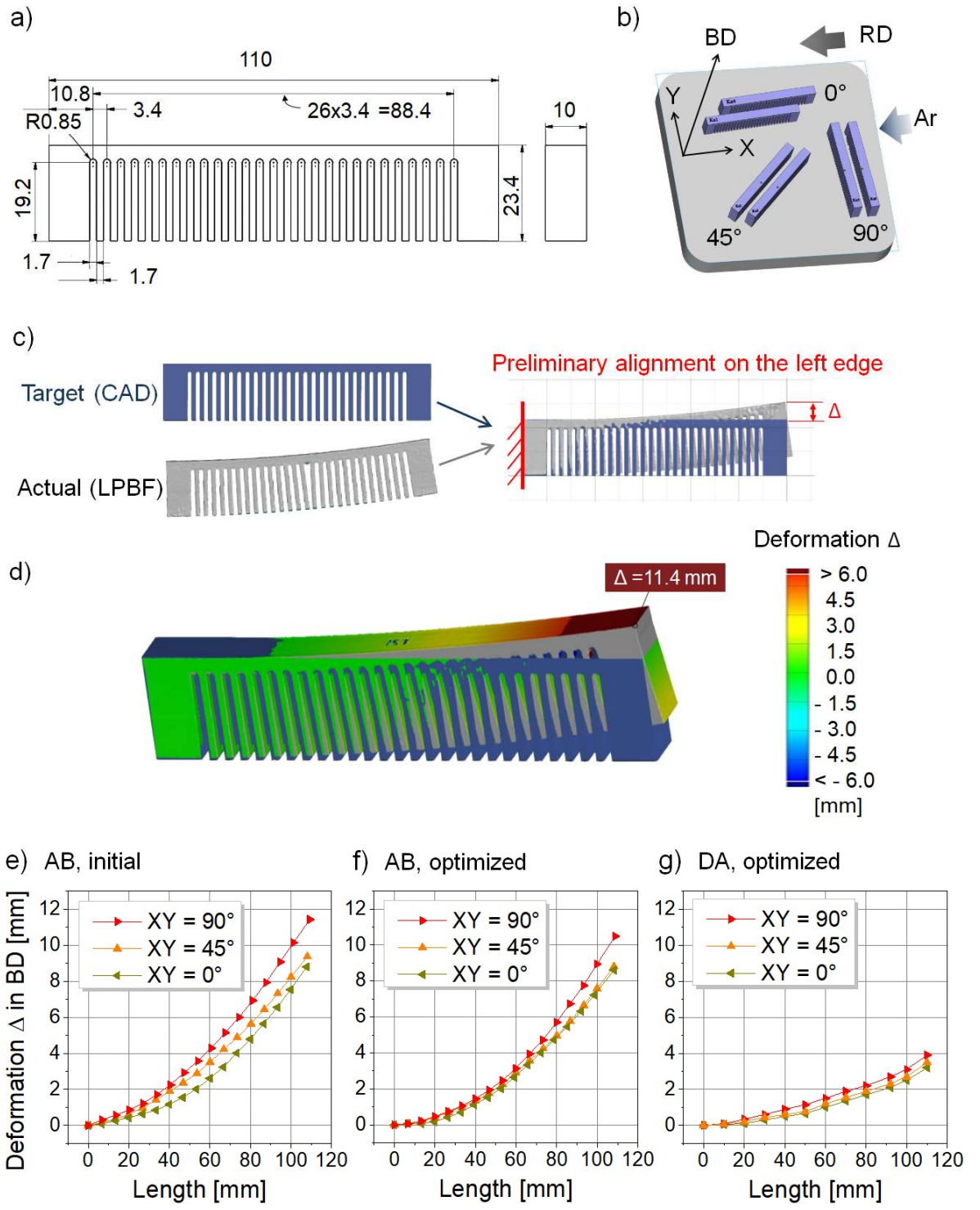

Fig. S4. Residual stress assessment: specimen geometry (a), variational horizontal arrangement on the working platform at angles XY = 0°, 45° and 90°, where BD, RD and Ar are directions of building, recoating and argon gas flow (b), estimation method by measuring the vertical deformation of the "Actual" LPBF samples along the length compared to the CAD model ("Target") when fixing the left edge (c), example of deformation calculation using GOM (d), comparative diagrams of deformation along the length for the AB state produces with initial (e) and optimized (f) process parameters and treated DA state (g) for optimized ones.

Section S3:

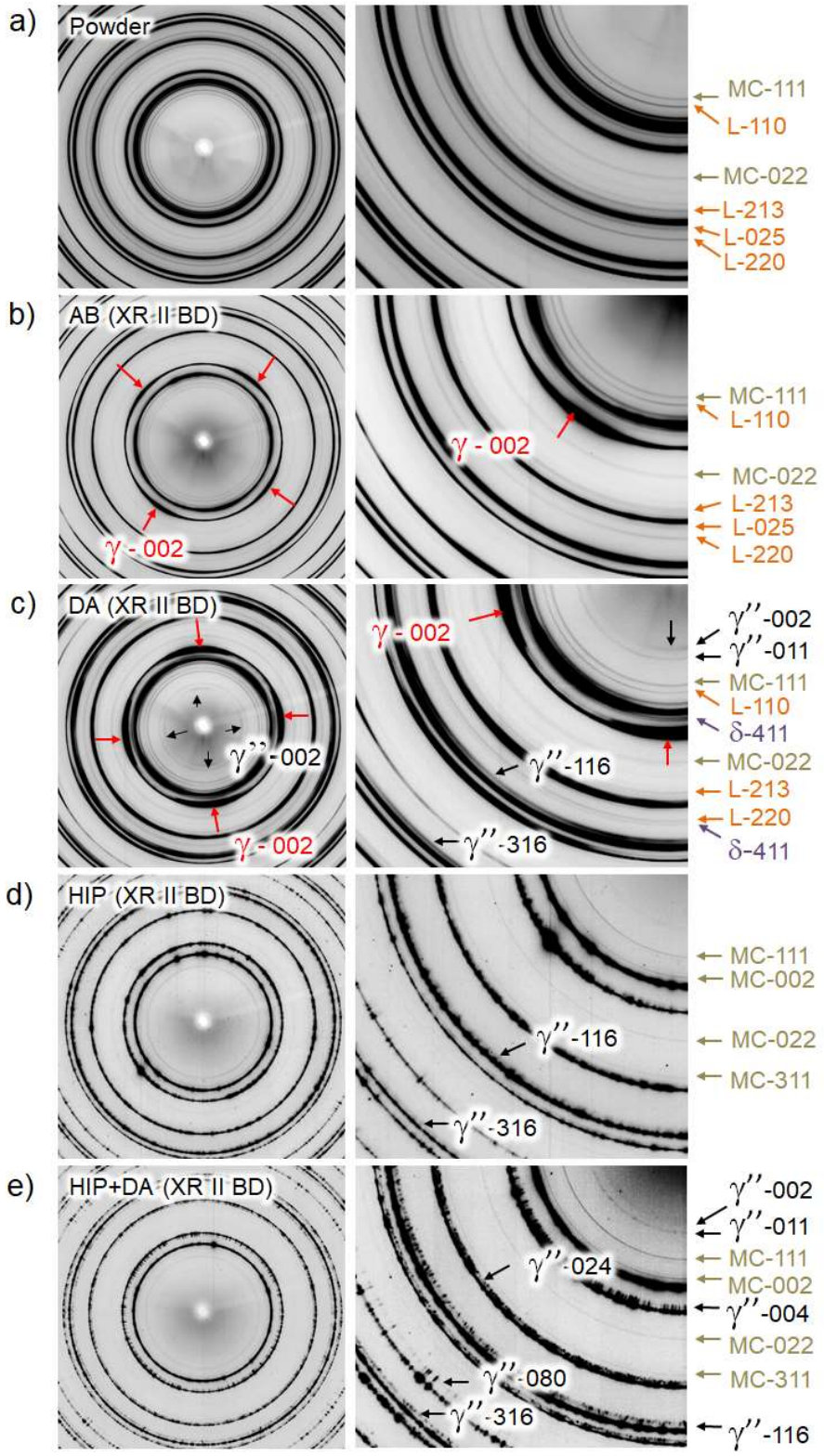

Fig. S5. Phase identification from HEXRD experiments as Debye-Scherrer rings for the IN718 powder (a), LPBF IN718 AB (b) and the DA, HIP and HIP+DA heat-treated states (c, d, e, respectively) for the ∥ to the BD structures.

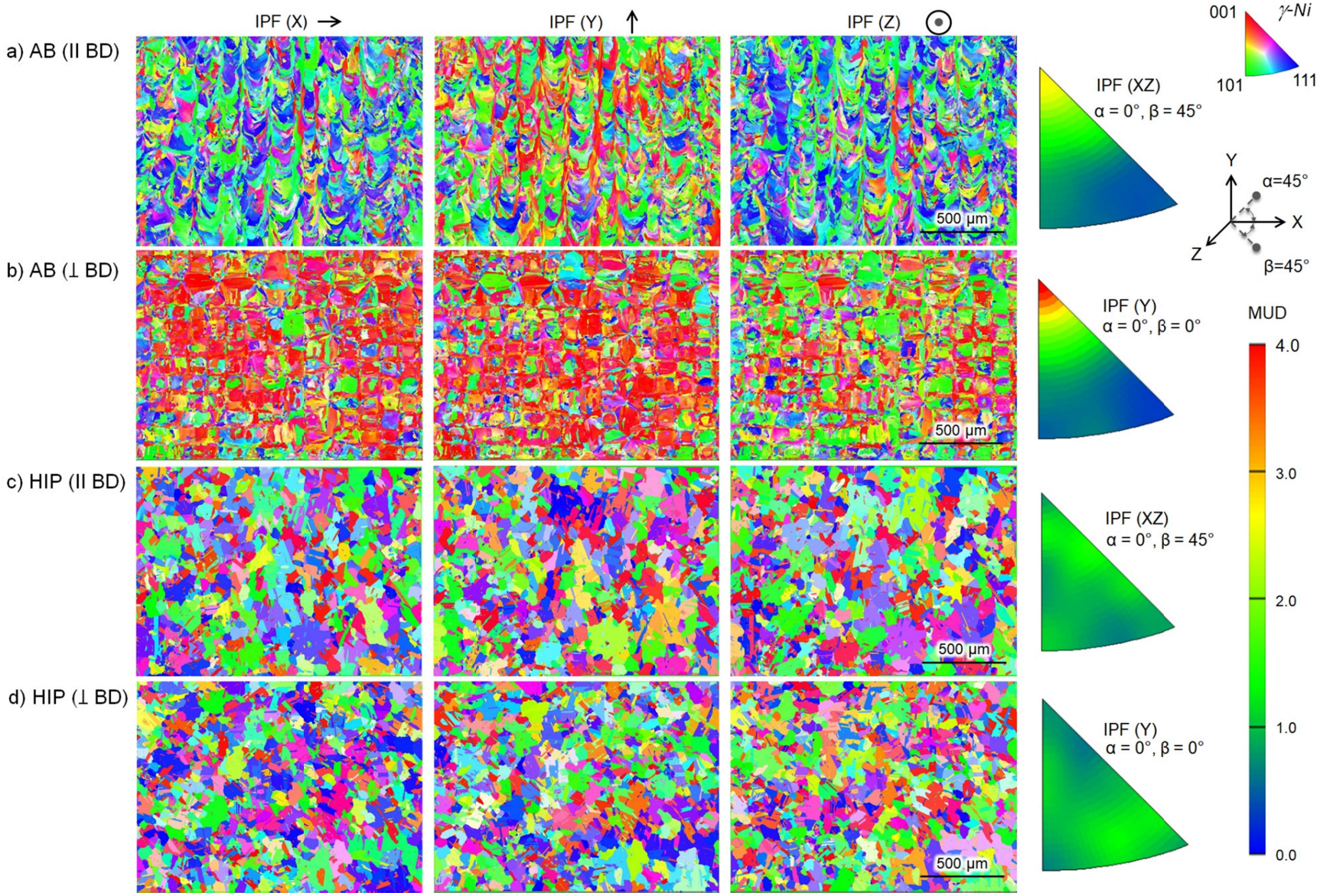

Fig. S6. EBSD IPF maps and corresponding IPF for the preferred <100> orientation: (a) AB (∥ BD corresponding to IPF (Y), IPF(XZ))

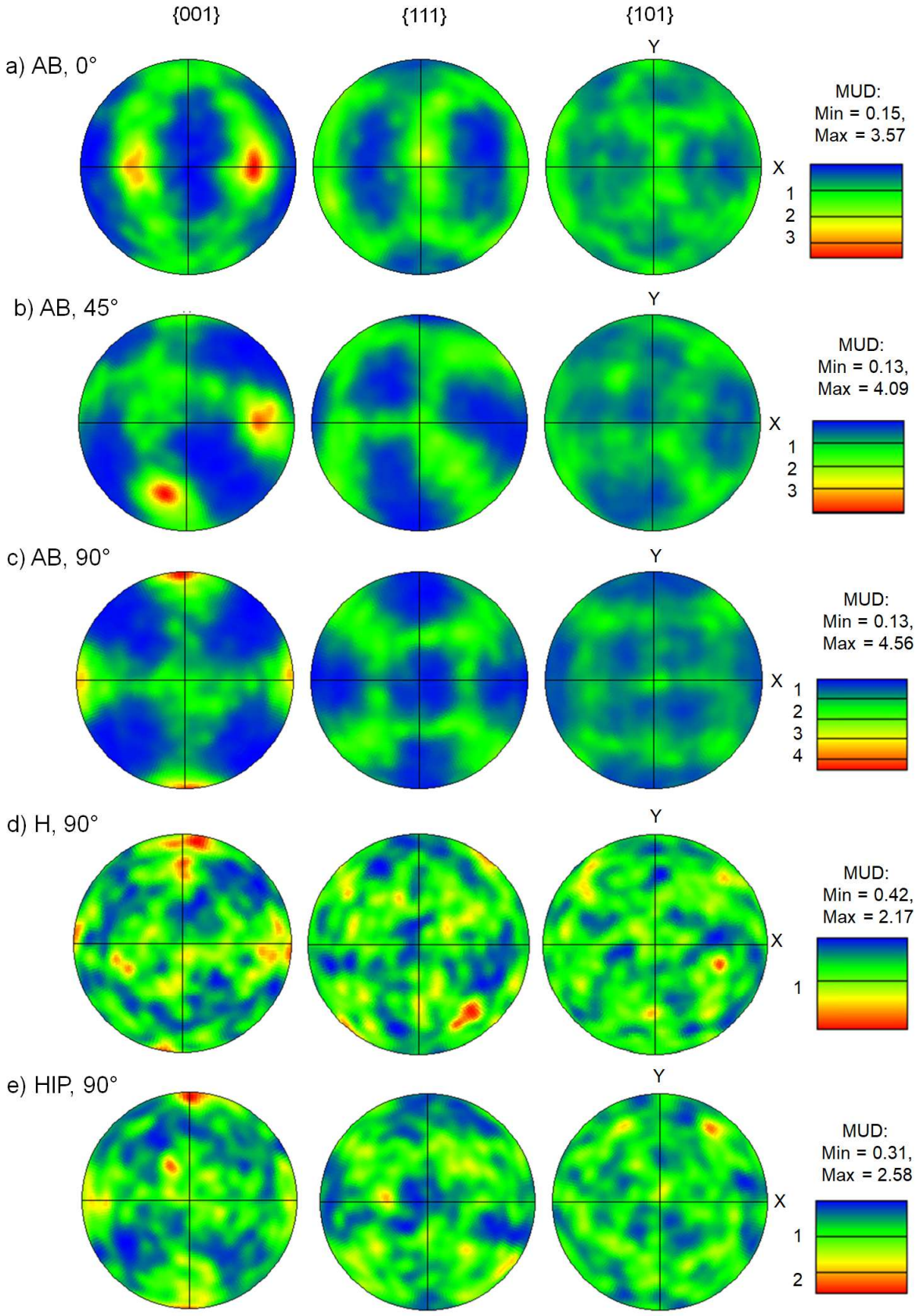

Fig. S7. Pole figures and MUD values for the LPBF IN718 states derived from the EBSD measurements: AB, 0° (a), AB, 45° (b), AB, 90° (c), H,90° (d) and HIP, 90° (e).

Section S4: Tensile Testing

Table S1. Yield (YS) and tensile strength (UTS), Young´s modulus (E) and elongation to failure (ε_f) of the AB and heat-treated LPBF IN718 specimens produced in 0° (horizontal), 45° (diagonal) and 90° (vertical) orientations to the building platform (**Fehler! Verweisquelle konnte nicht gefunden werden.**).

Material condition	Built direction	YS [MPa]	UTS [MPa]	E [GPa]	ε_f [%]
AB	0°	855 ± 4	1119 ± 2	217 ± 5	29.7 ± 1.3
	45°	787 ± 4	1090 ± 2	211 ± 12	31.5 ± 1.3
	90°	625 ± 8	1006 ± 3	195 ± 6	38.1 ± 0.4
	Average	756 ± 118	1072 ± 59	208 ± 11	33.1 ± 4.4
DA	0°	1445 ± 1	1573 ± 1	211 ± 3	11.8 ± 1.0
	45°	1415 ± 4	1547 ± 3	189 ± 7	10.7 ± 1.5
	90°	1293 ± 9	1454 ± 3	181 ± 8	12.8 ± 1.1
	Average	1384 ± 81	1525 ± 63	194 ± 16	11.8 ±1.1
H	0°	923 ± 8	1284 ± 7	196 ± 1	32.9 ± 0.4
	45°	915 ± 5	1263 ± 3	211 ± 10	29.8 ± 1.4
	90°	898 ± 6	1238 ± 6	195 ± 6	30.6 ± 1.7
	Average	912 ± 13	1262 ± 23	201 ± 9	31.1 ±1.6
H+DA	0°	1194 ± 5	1421 ± 2	193 ± 16	24.9 ± 0.2
	45°	1173 ± 2	1394 ± 2	184 ± 3	20.9 ± 2.5
	90°	1147 ± 0	1365 ± 4	193 ± 8	22.0 ± 2.6
	Average	1171 ± 24	1393 ± 28	190 ± 5	22.6 ± 2.1
HIP	0°	798 ± 4	1198 ± 3	203 ± 9	42.0 ± 0.4
	45°	771 ± 2	1169 ± 1	192 ± 2	41.8 ± 0.4
	90°	762 ± 4	1142 ± 3	192 ± 7	44.8 ± 0.8
	Average	777 ± 19	1170 ±28	196 ±6	42.9 ± 1.7
HIP+DA	0°	1212 ± 4	1419 ± 4	194 ± 3	23.1 ± 2.7
	45°	1188 ± 9	1401 ± 5	187 ± 10	28.5 ± 1.1
	90°	1167 ± 4	1374 ± 1	179 ± 3	30.2 ± 1.4
	Average	1189 ± 23	1398 ±23	187 ± 8	26.2 ± 5.6